

Multidimensional adaptive order GP-WENO via kernel-based reconstruction

Ian May^a, Dongwook Lee^a

^a*Department of Applied Mathematics, The University of California, Santa Cruz, CA, United States*

Abstract

This paper presents a fully multidimensional kernel-based reconstruction scheme for finite volume methods applied to systems of hyperbolic conservation laws, with a particular emphasis on the compressible Euler equations. Non-oscillatory reconstruction is achieved through an adaptive order weighted essentially non-oscillatory (WENO-AO) method cast into a form suited to multidimensional stencils and reconstruction. A kernel-based approach inspired by Gaussian process (GP) modeling is presented here. This approach allows the creation of a scheme of arbitrary order with simply defined multidimensional stencils and substencils. Furthermore, the fully multidimensional nature of the reconstruction allows a more straightforward extension to higher spatial dimensions and removes the need for complicated boundary conditions on intermediate quantities in modified dimension-by-dimension methods. In addition, a new simple-yet-effective set of reconstruction variables is introduced, as well as an easy-to-implement effective limiter for positivity preservation, both of which could be useful in existing schemes with little modification. The proposed scheme is applied to a suite of stringent and informative benchmark problems to demonstrate its efficacy and utility.

Keywords: Finite volume method
High-order methods
Kernel-based reconstruction
Gaussian process modeling
Multidimensional WENO
Compressible Euler equation

1. Introduction

The numerical solution of systems of hyperbolic conservation laws has been a vigorous subject of research for several decades now. A notable feature of hyperbolic conservation laws is their ability to simultaneously support complicated – but otherwise smooth – solutions and discontinuous solutions. The nonlinear nature of the hyperbolic laws can potentially turn initially smooth flows into non-smooth flows with shocks and discontinuities. We seek to numerically solve hyperbolic conservation laws in divergence form

$$\frac{\partial \mathbf{U}}{\partial t} + \nabla \cdot \mathbf{F}(\mathbf{U}) = 0, \quad (1)$$

where \mathbf{U} is a vector of conserved variables and \mathbf{F} is convex flux tensor. In particular, we focus on the two dimensional compressible Euler equations defined by

$$\mathbf{U} = \begin{pmatrix} \rho \\ \rho u \\ \rho v \\ E \end{pmatrix}, \quad \mathbf{F} = \left\{ \begin{pmatrix} \rho u \\ \rho u^2 + P \\ \rho uv \\ u(E + P) \end{pmatrix}, \begin{pmatrix} \rho v \\ \rho uv \\ \rho v^2 + P \\ v(E + P) \end{pmatrix} \right\}, \quad (2)$$

where the conserved quantities are the density, linear momenta, and total energy, respectively. This equation is closed by the adiabatic equation of state for the pressure $P = (\gamma - 1) \left(E - \frac{1}{2} \rho (u^2 + v^2) \right)$, where γ is the adiabatic constant.

Numerical methods for the solution of these systems thus need to be designed around at least two competing goals: (i) accurate representation and evolution of smooth solutions and (ii) robust physically consistent behavior in the vicinity of discontinuities. Modern computer hardware strongly favors the use of high-order accurate schemes that promote increased floating point operations for accuracy to efficiently resolve smooth solutions. On the other hand, Godunov's theorem [1] asserts that these methods must be inherently nonlinear if they are to be stable.

Essentially non-oscillatory (ENO) schemes [2, 3], and subsequently weighted essentially non-oscillatory (WENO) schemes [4, 5] have been one fruitful avenue for the design of methods that can simultaneously handle smooth data gracefully and discontinuous data robustly. There are a number of different variants in WENO, which aim to improve the baseline WENO scheme of Jiang and Shu [5] (WENO-JS). Examples include WENO-Z [6, 7], central-WENO [8, 9, 10], Hermite-WENO [11, 12], WENO-AO [13], mapped WENO [14, 15, 16, 17, 18, 19], and more recently polynomial-free kernel-based GP-WENO [20, 21]. Finite difference methods readily generalize to higher dimensions by applying baseline one-dimensional schemes in a dimension-by-dimension manner (e.g., see [21]), which preserves the target one-dimensional solution accuracy in higher dimensions easily. The simple nature of such extensibility of accuracy to higher spatial dimensions is mainly due to the fact that finite difference methods evolve pointwise quantities, providing ease of code development in practice. In comparison, finite volume methods evolve volume-averaged (or cell-averaged) quantities, which requires attentive mathematical considerations, particularly in designing spatial reconstruction schemes, to demonstrate high-order accuracy in multiple spatial dimensions [22, 23, 24, 25]. Numerical solutions of multidimensional finite volume methods with a naive dimension-by-dimension spatial reconstruction will be limited to second-order [26, 27, 28].

Apart from the main attention on multidimensional reconstruction schemes, at the core of these schemes are key mathematical components that distinguish them from and improve upon the baseline WENO-JS, featuring enhanced accuracy on smooth flows, elaborate nonlinear strategies for suppressing oscillatory solutions near discontinuities, efficient use of compact stencils, to name a few. While in most cases, their novel developments are now quite mature in one-dimensional cases, their multidimensional counterparts are often obtained by a dimension-by-dimension formalism in practice. These are either limited to second-order accuracy, or involve further efforts to tie these one-dimensional reconstructions together in an appropriately multidimensional fashion.

A few key challenges arise in the development of multidimensional polynomial WENO schemes. Several practitioners have taken multivariate polynomials to design novel high-order schemes [23, 24]. In general, however, multidimensional interpolation/reconstruction suffers from the well-known complications where not all stencils result in a well-conditioned or solvable linear system. The full stencil should be as small as possible while allowing the reconstruction of a polynomial of the desired degree for accuracy. The full stencil should also be symmetric with respect to the grid to avoid having any preferred direction and allow decomposition into symmetrically placed substencils. The size and shape of the substencils also need to support the desired k^{th} degree multivariate polynomial reconstruction compatible with the full stencil. Matching the full stencil and substencil sizes to the dimension of polynomial spaces while satisfying the symmetry requirements is generally impossible. The use of rectangular stencils allows reconstruction in a tensor product basis at the cost of larger stencils than necessary to reach a given order of accuracy. Alternatively, one could reconstruct polynomials in the least squares sense by using more cells per (sub)stencil than the dimension of the corresponding space of polynomials. See more discussions in [25, 29].

One-dimensional reconstructions can be bootstrapped into higher dimensions while maintaining accuracy by performing transverse corrections [30]. In this type of scheme, cell-averaged quantities are first used to reconstruct face-averaged quantities, which are subsequently used as input to a second reconstruction in the transverse direction to recover (i.e., reconstruct) point values on the faces. Referred to as Riemann states, these point values are, by design, to be constructed to attain not only high-order accuracy but also sufficient numerical stability in multiple dimensions. This approach is generally cheaper than fully multidimensional reconstruction but suffers several essential drawbacks: (i) reconstruction of the Riemann states now requires multiple directional passes over the data, (ii) near the domain boundaries, the *intermediate* face-averaged quantities need to be filled in accordance with the boundary conditions, which may be non-trivial, and (iii) implementations relying on distributed memory parallelism need to either perform additional communications to fill these face-averaged quantities in neighboring subdomains or localize communication by utilizing sufficiently large overlaps to repeat work adjacent to the local subdomain. In two dimensions, these drawbacks complicate the implementation mildly but are otherwise manageable. However, all of these issues are compounded in three dimensions where three passes over the data and two intermediate quantities are required, e.g., the first reconstruction from the three-dimensional volume-averaged quantities (triple-integral quantities) to face-averaged quantities (double-integral quantities), then the second reconstruction from the face-averaged quantities to line-averaged quantities (single-integral quantities), followed by the third reconstruction from the line-averaged quantities to pointwise quantities finally. These complications and the desire for a method that generalizes to higher dimensions with minimal modification motivate the present investigation.

Taking a kernel-based approach to reconstruction alleviates many of these issues. The global stencil and substencils can be chosen with size and symmetry as the primary motives. The accuracy of reconstruction (or interpolation) on any (sub)stencil is determined by what polynomials can be *reproduced* there by the chosen kernel and stencil. Kernel-based reconstruction can be seen as a generalization of the least squares

approach to polynomial reconstruction, where the polynomial spaces assigned to each (sub)stencil are implicitly defined [31, 32]. This greatly simplifies the design and implementation of schemes with generic orders of accuracy. Furthermore, during each reconstruction process, only the cell-averaged values (i.e., the initial states) and the Riemann states (i.e., the final states) themselves need to be filled with respect to the boundary conditions. No intermediate quantities need to be filled in accordance with the boundary conditions or from other processes in a distributed memory setting. Although we present only two-dimensional benchmarks, the method generalizes to three dimensions readily.

The present study builds around a series of recent works exploring the kernel-based Gaussian Process (GP) approach as an alternative to traditional polynomial-based approaches. The first shock-capturing finite volume (FV) GP algorithm was introduced in [20]. Called GP-WENO, this study put forward a new way of designing a versatile selectable-order property in modeling the 1D Euler equations. In addition to the newly proposed one-dimensional GP reconstruction scheme therein, this work also refactored the conventional L_2 -based *a priori* shock-handling smoothness indicators for polynomial WENO reconstruction [5] into an alternative that is genuinely designed for polynomial-free GP reconstruction. The GP paradigm has also been successfully developed in a finite difference method (FDM). Interested readers can refer to the work [21], where a full three-dimensional conservative GP-WENO finite difference scheme solves a stringent set of benchmark problems in the system of the Euler equations with improved solution accuracy and computational efficiency. The shock-capturing strategy of the aforementioned GP schemes bears the form of the so-called *a priori* nonlinear limiting, in which some types of nonlinear shock-detecting procedures are put in place to avoid oscillations near shocks and discontinuities. Following this traditional pathway, the above GP solvers rely on the WENO-type of nonlinear shock handling limiters that are applied all over the grid. Unlike these *a priori* GP-WENO methods, a two-dimensional *a posteriori* GP-MOOD (Multidimensional Optimal Order Detection) scheme in finite volume has been studied and reported in [25]. GP-MOOD adopts a set of high-order GP reconstruction methods (e.g., 3rd, 5th, and 7th) in place of the polynomial reconstructions in the original polynomial-MOOD approach [33, 34, 35, 36]. The resulting method is a strong positivity-preserving GP-based solver for shock-dominant compressible flows. This new GP-MOOD further improves upon the ingredients of the original MOOD limiting in the polynomial MOOD methods [33, 34, 35, 36] by introducing the new Compressibility-Shock Detection switch that controls a good balance between numerical accuracy and diffusivity. Besides, there have been other types of GP applications beyond its fundamental role as a hyperbolic solver. In the recent work [29] by Reeves *et al.*, the GP-WENO method was extended to a 3rd-order prolongation algorithm in finite volume adaptive mesh refinement (AMR) simulations using AMReX [37]. As another application, in [38], the GP interpolation was shown as an improved mathematical tool that enhances optical characters in coarse resolutions to upsampled characters in refined resolutions.

This paper proceeds as follows. Section 2 reviews kernel-based interpolation and reconstruction. Section 3 extends this reconstruction scheme to incorporate WENO to handle discontinuous data and deliberates on the choice of variables for reconstruction. Section 4 then presents a simple, effective method for positivity preservation in the

context of the compressible Euler equations. Finally, the method in full is reviewed in Section 5, followed by a suite of benchmark problems in Section 6.

2. Overview of kernel reconstruction

The first principal component of a finite volume method for the solution of systems of conservation laws is the reconstruction of the state within each cell, which can then be evaluated to find high-order accurate pointwise-valued Riemann states along the boundary of the cell. This reconstruction, $\widetilde{U}(x)$, should simultaneously provide an accurate approximation of the true state and remain well-behaved in the presence of shocks or other discontinuities. In the present study, we pose this reconstruction problem as optimal recovery in a reproducing kernel Hilbert space (RKHS) [10, 31, 39]. This approach yields a form that is mostly dimension-independent and allows great flexibility in the choice of stencils. We note that related but distinct formulations have been examined previously [40, 41, 42, 43].

By convention, we refer to this RKHS approximation as *interpolation* when it matches given pointwise data. On the other hand, we refer to *reconstruction* (or generalized interpolation) as an operation that matches cell averages, or other more general input data. In this section, a kernel-based method for reconstruction is presented. Kernel interpolation is recalled first, and subsequently adapted to the reconstruction problem. The reconstruction presented here is *linear* (i.e., without any nonlinear limiting) with respect to the input data, and hence inappropriate for use near shocks. This is resolved in Section 3.

2.1. Kernel interpolation

Suppose point values of a function $f(\mathbf{x})$ are known at a (finite and distinct) set of points $\mathbf{x}_h \in \mathbb{R}^d$ for $h = 1, \dots, N$. Let us denote the known values as $[\mathbf{f}]_h = f(\mathbf{x}_h)$. Kernel *interpolation* seeks an interpolant $\widetilde{f}_{int}(\mathbf{x})$ of the form

$$\widetilde{f}_{int}(\mathbf{x}) = \sum_{l=1}^N \alpha_l K(\mathbf{x}, \mathbf{x}_l), \quad (3)$$

where $K : \mathbb{R}^d \times \mathbb{R}^d \rightarrow \mathbb{R}$ is a symmetric positive definite (SPD) kernel [31]. Requiring that this function interpolate the known values, $\widetilde{f}_{int}(\mathbf{x}_h) = [\mathbf{f}]_h$, yields a linear system for the coefficients α_l ,

$$\sum_{l=1}^N [\mathbf{K}]_{hl} \alpha_l = [\mathbf{f}]_h, \quad h = 1, \dots, N, \quad (4)$$

where $[\mathbf{K}]_{hl} = K(\mathbf{x}_h, \mathbf{x}_l)$, or equivalently,

$$\mathbf{K}\boldsymbol{\alpha} = \mathbf{f}, \quad (5)$$

in a compact form with the $N \times 1$ column vector $[\boldsymbol{\alpha}]_l = \alpha_l$. By virtue of $K(\mathbf{x}, \mathbf{y})$ being SPD and the points \mathbf{x}_h being distinct, the matrix \mathbf{K} will also be SPD, allowing the linear system Eq. (5) to be solved for $\boldsymbol{\alpha} = \mathbf{K}^{-1}\mathbf{f}$ using Cholesky decomposition to invert \mathbf{K}

in general as long as \mathbf{K} remains well-conditioned. In practice, \mathbf{K} could become ill-conditioned as the set of points $\{\mathbf{x}_h\}$ becomes increasingly dense, which we discuss our approach in Section 2.3.

The evaluation of this interpolant at a point, $\mathbf{x}^* \in \mathbb{R}^d$, is $\tilde{f}_{int}(\mathbf{x}^*) = \sum_{l=1}^N \alpha_l K(\mathbf{x}^*, \mathbf{x}_l)$. Note that the matrix \mathbf{K} in Eq. (4) depends only on the points \mathbf{x}_h and \mathbf{x}_l but not on the function data \mathbf{f} . We now define the $N \times 1$ *sample vector* \mathbf{S} with respect to \mathbf{x}^* as

$$[\mathbf{S}]_l = K(\mathbf{x}^*, \mathbf{x}_l), \quad (6)$$

which can be combined with Eq. (4) to write $\tilde{f}_{int}(\mathbf{x}^*)$ directly in terms of the known data \mathbf{f} weighted by $\mathbf{S}^T \mathbf{K}^{-1}$ as

$$\tilde{f}_{int}(\mathbf{x}^*) = \mathbf{S}^T \mathbf{K}^{-1} \mathbf{f}. \quad (7)$$

Note here that the vector $\mathbf{i}^T = \mathbf{S}^T \mathbf{K}^{-1}$, referred to as the *prediction vector* for kernel interpolation, is independent of the data, whereby it can be precomputed, saved, and reused to interpolate any given data \mathbf{f} from the point set $\{\mathbf{x}_h\}$ to the point \mathbf{x}^* via Eq. (7).

2.2. Kernel reconstruction

The above interpolation procedure can easily be adapted to the case where the input data consists of cell average quantities. Consider a set of finite volumes $\Omega_h \subset \mathbb{R}^d$ for $h = 1, \dots, N$, each with volume $\|\Omega_h\|$. Let us denote the cell averaging functional for Ω_h with respect to \mathbf{x} by

$$\lambda_h^{(\mathbf{x})} = \frac{1}{\|\Omega_h\|} \int_{\Omega_h} \cdot d\mathbf{x}. \quad (8)$$

The given data for reconstruction are given as cell averages of $f(\mathbf{x})$ which we gather into the vector \mathbf{g} whose entries are $[\mathbf{g}]_h = \lambda_h^{(\mathbf{x})} f(\mathbf{x})$. Similar to the kernel interpolation of pointwise data in Eq. (3), symmetric kernel *reconstruction* seeks an approximant of the form

$$\tilde{f}_{rec}(\mathbf{x}) = \sum_{l=1}^N \alpha_l \lambda_l^{(\mathbf{y})} K(\mathbf{x}, \mathbf{y}). \quad (9)$$

Then, enforcing that Eq. (9) is exact for the given cell-averaged data \mathbf{g}_h , i.e.,

$$\lambda_h^{(\mathbf{x})} \tilde{f}_{rec}(\mathbf{x}) = \lambda_h^{(\mathbf{x})} f(\mathbf{x}) = [\mathbf{g}]_h, \quad (10)$$

yields a linear system for the coefficients α_l as

$$\sum_{l=1}^N [\mathbf{C}]_{hl} \alpha_l = [\mathbf{g}]_h, \quad h = 1, \dots, N, \quad (11)$$

where the matrix \mathbf{C} has entries given by

$$[\mathbf{C}]_{hl} = \lambda_h^{(\mathbf{x})} \lambda_l^{(\mathbf{y})} K(\mathbf{x}, \mathbf{y}) = \frac{1}{\|\Omega_h\| \|\Omega_l\|} \int_{\Omega_h} \int_{\Omega_l} K(\mathbf{x}, \mathbf{y}) dy dx. \quad (12)$$

The matrix \mathbf{C} again is SPD so long as the functionals $\lambda_s^{(\xi)}$ are linearly independent for each $\xi = \mathbf{x}, \mathbf{y}$ and $s = 1, \dots, N$. Including the averaging functional $\lambda_l^{(\mathbf{y})}$ in the expansion in Eq. (9) is not required but serves to symmetrize the linear system [44]. Note that one could use the expansion Eq. (3) and impose the constraints $\lambda_h^{(\mathbf{x})} \widetilde{f}_{int}(\mathbf{x}) = \lambda_h^{(\mathbf{x})} f(\mathbf{x}) = [\mathbf{g}]_h$. The resulting linear system is no longer symmetric since $\lambda_h^{(\mathbf{x})} K(\mathbf{x}, \mathbf{x}_l) \neq \lambda_l^{(\mathbf{x})} K(\mathbf{x}, \mathbf{x}_h)$ generally. Note also that replacing the averaging functionals with point evaluation functionals recovers exactly the kernel interpolation problem presented in the previous section.

The evaluation of this reconstructed function \widetilde{f}_{rec} at some point $\mathbf{x}^* \in \mathbb{R}^d$ proceeds in much the same way as in the kernel interpolation case. Defining the *sample vector* with respect to $\mathbf{x}^* \in \mathbb{R}^d$ as

$$[\mathbf{T}]_l = \lambda_l^{(\mathbf{y})} K(\mathbf{x}^*, \mathbf{y}) = \frac{1}{\|\Omega_l\|} \int_{\Omega_l} K(\mathbf{x}^*, \mathbf{y}) d\mathbf{y}, \quad (13)$$

we obtain our anticipated high-order GP reconstruction at \mathbf{x} ,

$$\widetilde{f}(\mathbf{x}^*) = \mathbf{T}^T \mathbf{C}^{-1} \mathbf{g}. \quad (14)$$

Once again, for a given mesh resolution, \mathbf{T} and \mathbf{C} are completely independent of the data \mathbf{g} ; hence the vector

$$\mathbf{r}^T = \mathbf{T}^T \mathbf{C}^{-1}, \quad (15)$$

referred to as the *prediction vector* for kernel reconstruction, can be readily precomputed and saved. This way, during each simulation resolved on the given mesh resolution, the stored \mathbf{r}^T will then be reused without needing to be calculated.

2.3. Contour-Padé method for ill-conditioned systems

It should be noted that the matrices \mathbf{K} in Eq. (4) or \mathbf{C} in Eq. (12) is typically very ill-conditioned due to the flatness of the kernel function relative to the grid scale, which is described by the term ℓ/Δ in Section 3.1. Hence, directly inverting \mathbf{C} (or \mathbf{K}) to obtain the prediction vector \mathbf{r}^T (or \mathbf{i}^T) is likely to fail when the computational grid is highly refined with $\Delta \rightarrow 0$ or the kernel hyperparameter $\ell \rightarrow \infty$.

In our previous GP studies [20, 21, 25], we utilized quadruple precision floating-point arithmetic within only a small fraction of routines associated with the calculation of the prediction vector, including the corresponding Cholesky decomposition to invert the kernel matrix and the matrix and vector multiplication to obtain the prediction vector itself. As fully described therein, this approach has no negative impact since calculating the prediction vector is required only once at the initial step and is then saved in double precision for use in all further calculations.

Alternatively, many stable inversion schemes have been proposed [45, 46, 47, 48], largely coming from the radial basis function (RBF) literature. Most of these have been developed with RBF interpolation in mind, which matches the presentation in Section 2.1, particularly when $K(\mathbf{x}, \mathbf{y}) = \phi(\|\mathbf{x}, \mathbf{y}\|)$ is a radial kernel.

In this study, we utilize the Contour-Padé method [46] to stably invert the matrix \mathbf{C} for kernel reconstruction and to obtain the prediction vector \mathbf{r}^T . This method readily generalizes to the reconstruction case where the averaging functionals are applied symmetrically as in Eq. (12), as well as to the use of non-radial kernels.

2.4. Particularities of FVM reconstruction

The preceding discussions of kernel interpolation and reconstruction in Sections 2.1 and 2.2 are entirely general with respect to the kernel function and layout of input data. However, in this section, we show that the setup in the present study provides several significant simplifications as we focus on developing a finite volume scheme on a uniform structured grid.

First, the stencil shape for reconstruction can be chosen independent of the cell where reconstruction is being performed. This means that the prediction vector $\mathbf{r}^T = \mathbf{T}^T \mathbf{C}^{-1}$ depends only on the location of the evaluation point \mathbf{x}^* relative to the local cell where reconstruction is being done. Thus all cells will use the same few prediction vectors to evaluate Riemann states. The precomputation of \mathbf{r}^T incurs only a small fixed cost, where the cost itself is insignificant compared to the overall simulation times and is completely independent of differing mesh resolutions.

Second, the elemental finite volumes are all rectilinear, and the integration in Eq. (12) can be substantially simplified by choosing a separable (tensor-product) kernel. In this case, the multidimensional kernel K is induced by some one dimensional baseline kernel K_1 and is written as $K(\mathbf{x}, \mathbf{y}) = \prod_{k=1}^d K_1(x_k, y_k)$. The separability allows the entries of \mathbf{C} to be written as the product of d double integrals instead of one monolithic integral in \mathbb{R}^{2d} . Below, we emphasize that a tensor-product kernel does not in any way require tensor-product stencils.

Given these simplifications and the restriction to 2D, we let $\mathbf{x} = (x_1, x_2), \mathbf{y} = (y_1, y_2) \in \mathbb{R}^2$ and consider three different kernels

$$K_{se}(\mathbf{x}, \mathbf{y}; \ell) = e^{-\frac{\|\mathbf{x}-\mathbf{y}\|^2}{2\ell^2}} = e^{-\frac{(x_1-y_1)^2}{2\ell^2}} e^{-\frac{(x_2-y_2)^2}{2\ell^2}}, \quad (16)$$

$$K_{iq}(\mathbf{x}, \mathbf{y}; \ell) = \left(1 + \frac{(x_1 - y_1)^2}{\ell^2}\right)^{-1} \left(1 + \frac{(x_2 - y_2)^2}{\ell^2}\right)^{-1}, \quad (17)$$

$$K_{mq}(\mathbf{x}, \mathbf{y}; \ell) = \sqrt{1 + \frac{(x_1 - y_1)^2}{\ell^2}} \sqrt{1 + \frac{(x_2 - y_2)^2}{\ell^2}}, \quad (18)$$

where the hyperparameter ℓ is a characteristic length scale. The first kernel K_{se} is the *squared exponential* (SE) kernel, which is radial (i.e., depends only on the Euclidean distance $\|\mathbf{x} - \mathbf{y}\|$) and separable regardless of d . The latter two are separable versions of the familiar *inverse quadratic* (IQ) and *multiquadric* (MQ) kernels [32, 49]; however, these kernels are no longer radial for $d > 1$. The action of the cell averaging functionals $\lambda_s^{(\xi)}$ for each ξ and s in Eq. (12) and Eq. (13) can be computed analytically for the K_{se} kernel using the error function (e.g., see [25] and Appendix A). Such analytical integration is not available for the K_{iq} and K_{mq} kernels, and an accurate numerical integration method needs to be used instead. In the latter case, we use a 9-point Gauss-Legendre rule.

The kernels K_{se} and K_{iq} are both symmetric and positive definite, the latter being the tensor product of positive definite one-dimensional kernels [32, 49]. However, K_{mq} is only conditionally positive definite and the induced matrices \mathbf{K} and \mathbf{C} could be singular for certain sets $\{\mathbf{x}_h\}$ or $\{\Omega_h\}$. The typical way to handle this deficiency is to add global polynomials up to the order of conditional positive definiteness to the

expansions Eq. (3) and Eq. (9). Alternatively, one can simply ignore the fact that these kernels are not strictly positive definite, which is the approach we take here. This is justified in that we are not considering arbitrary $\{\mathbf{x}_h\}$ or $\{\mathbf{\Omega}_h\}$, but rather a few fixed stencils over which \mathbf{K} and \mathbf{C} are known to be nonsingular [49].

We note that these interpolation and reconstruction methods can also be interpreted as evaluations of the *updated posterior predictive mean* of a Gaussian process in the zero-noise limit [40, 21, 25, 49, 50, 51]. In this case, the matrices defined in Eq. (4) and Eq. (12) are viewed as the *covariance matrices*, which equivalently produce the same sample vectors and prediction vectors as presented in Sections 2.1 and 2.2.

We make another consequential remark on the GP reconstruction. Viewing the reconstruction procedure through the lens of Gaussian processes could provide insight into the optimization of the length scale ℓ , and possibly into uncertainty quantification via an updated posterior covariance kernel [50, 51]. As length scale optimization and uncertainty quantification lie beyond the scope of this work, the remainder of this paper will only concern the *deterministic* interpretation of kernel reconstruction.

3. Kernel-based Multidimensional GP-WENO

The above reconstruction scheme is linear with respect to the input data, which will unavoidably generate unwanted oscillations in the vicinity of discontinuities. In this section, a weighted essentially non-oscillatory (WENO) scheme is developed for these kernel-based reconstructions to control such oscillations. The great flexibility of kernel-based reconstruction allows many different stencil and substencil configurations.

3.1. Stencils and substencils

We consider ‘‘circular’’ stencils of radius $R \geq 2$ which give reconstructions accurate to order $\mathcal{O}(h^{2R+1})$ with the grid delta $h = \min\{\Delta x, \Delta y\}$. Examples can be seen in Fig. 1 and Fig. 2 for $R = 2$ and $R = 3$, respectively. Let $\mathcal{S}_0 = \{(i, j) \in \mathbb{Z}^2 : (i^2 + j^2) \leq R^2\}$ denote the full circular stencil of radius R , indexed relative to the central cell where $(i, j) = (0, 0)$ and reconstruction is being performed. This full stencil \mathcal{S}_0 is then broken into five substencils $\mathcal{S}_k, k = 1, \dots, 5$, consisting of one central substencil of smaller radius, \mathcal{S}_1 , and four biased substencils, $\mathcal{S}_2, \dots, \mathcal{S}_5$, given as:

$$\mathcal{S}_1 = \{(i, j) \in \mathcal{S}_0 : (i^2 + j^2) \leq (R - 1)^2\}, \quad (19)$$

$$\mathcal{S}_2 = \{(i, j) \in \mathcal{S}_0 : |j| \leq i\}, \quad (20)$$

$$\mathcal{S}_3 = \{(i, j) \in \mathcal{S}_0 : |j| \leq -i\}, \quad (21)$$

$$\mathcal{S}_4 = \{(i, j) \in \mathcal{S}_0 : |i| \leq j\}, \quad (22)$$

$$\mathcal{S}_5 = \{(i, j) \in \mathcal{S}_0 : |i| \leq -j\}. \quad (23)$$

For a given point \mathbf{x}^* in the central cell where point values are to be reconstructed, Eq. (13) and Eq. (14) furnish a different linear weight vector for each (sub)stencil. Calculated by Eq. (15), we denote the k^{th} such prediction vector by $\mathbf{r}^{(k)}$ on \mathcal{S}_k for each $k = 0, \dots, 5$. Note that the stencil, as written, consists of a collection of unit squares rather than cells matching the grid scale $\Delta x \times \Delta y$. The integrals required for filling the

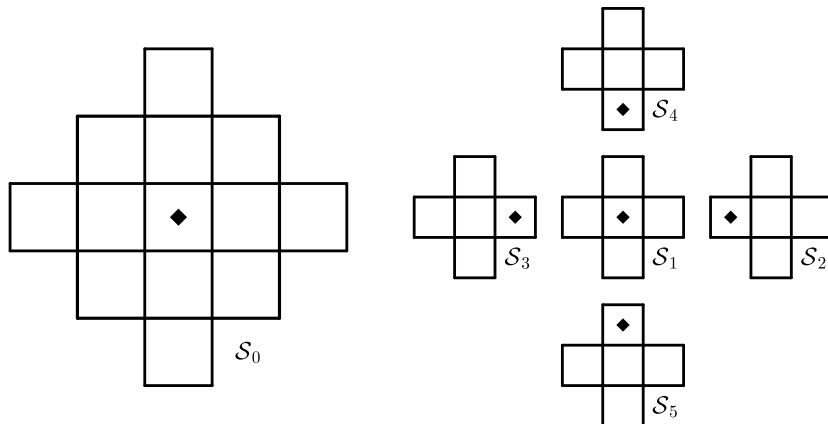


Figure 1: The full radius-2 stencil S_0 is shown on the left with its five substencils, $S_k, k = 1, \dots, 5$, on the right. The cell with the diamond in each (sub) stencil indicates the central cell where reconstruction is performed. The full stencil S_0 has 13 cells, while each of the substencils has five.

matrix in Eq. (12) and the sample vector in Eq. (13) are more easily calculated over these unit squares. This change of variables only requires that the length scale ℓ be replaced by ℓ/Δ inside the kernel. This change naturally cancels out the prefactor that scales by the cell volume and decouples the calculation of the prediction vectors from the description of the grid. Note that for grids with $\Delta x \neq \Delta y$, this reformulation will make the kernel anisotropic due to the presence of two different scales, $\ell/\Delta x$ and $\ell/\Delta y$. The Sod benchmark problem in Section 6.2 makes use of an anisotropic kernel. Additionally, this reformulation will be exploited to generate grid-independent smoothness indicators in Section 3.3.

3.2. Adaptive order WENO

A traditional WENO method leverages only the substencils (i.e., excluding the full stencil) to recover the action of the full stencil S_0 over smooth data *indirectly* through cleverly chosen nonlinear weights, often denoted as $\tilde{\omega}_k$ for unnormalized ones and ω_k for the associated normalized ones. In our GP-WENO reconstruction, however, this is only possible when the 0^{th} prediction vector $\mathbf{r}_{(0)}$ on S_0 lies in the span space of the remaining prediction vectors, i.e., $\mathbf{r}_{(0)} \in \text{span}\{\mathbf{r}_{(k)} : k = 1, \dots, N\}$, where N is the number of substencils. Here, the prediction vectors of the substencils, $\mathbf{r}_{(k)}, k = 1, \dots, N$, are to be appropriately extended by zero-paddings to match the dimension of $\mathbf{r}_{(0)}$. To construct nonlinear weights, linear weights, denoted as γ_k , must be determined first. To this end, inexact linear weights could be found by solving a least-squares problem (e.g., see [20] for a 1D GP-WENO in FVM and [40] for a multidimensional GP-WENO in FDM). Unfortunately, though, we have observed a degradation in accuracy when applying this approach to multidimensional FVM reconstruction; hence the least-squares approach is not appropriate for the current study.

Alternatively, the adaptive order WENO method (WENO-AO) employs the full stencil S_0 *directly* and selects weights solely to provide stability [52]. Given a vector

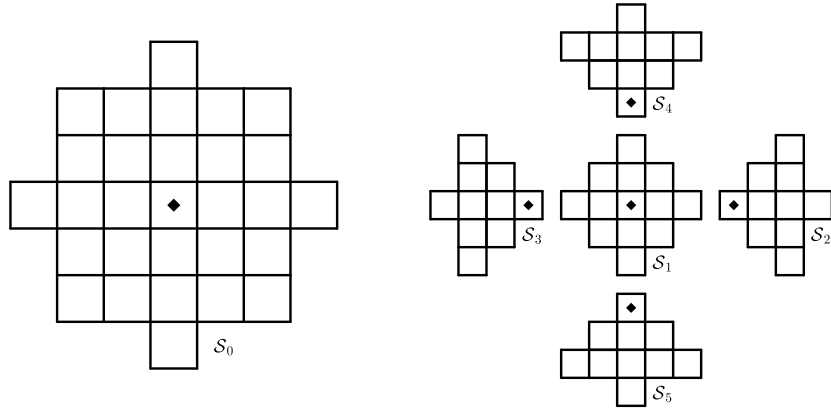


Figure 2: The full radius-3 stencil \mathcal{S}_0 is shown on the left with its five sub-stencils, $\mathcal{S}_k, k = 1, \dots, 5$, on the right. The cell with the diamond in each (sub)stencil indicates the central cell where reconstruction is being performed. The full stencil \mathcal{S}_0 has 29 cells, the central sub-stencil \mathcal{S}_1 has 13 cells, and each of the remaining biased sub-stencils, $\mathcal{S}_2, \dots, \mathcal{S}_5$, has 10.

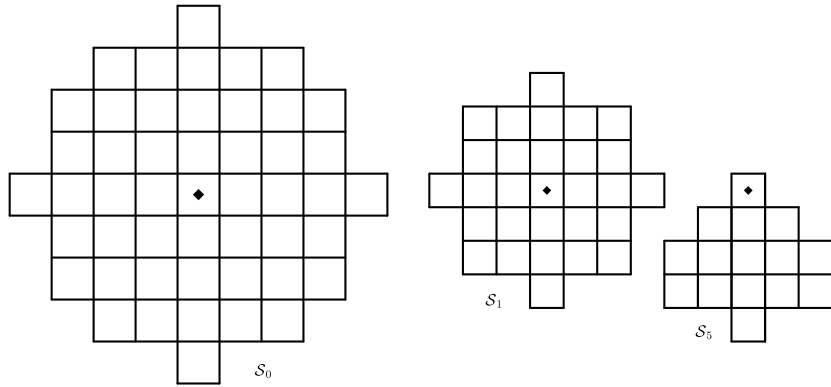


Figure 3: The full radius-4 stencil \mathcal{S}_0 containing 49 cells is shown on the left. As before, the full stencil \mathcal{S}_0 is subdivided into one central stencil \mathcal{S}_1 and four other biased stencils, $\mathcal{S}_k, k = 2, \dots, 5$. For the radius-4 case, the central stencil, \mathcal{S}_1 , depicted in the middle, contains 25 cells, while each of the four biased stencils contains 15 cells. Similar to the previous radius-2 and radius-3 cases, the four biased stencils join the full stencil \mathcal{S}_0 covering the equal sub-area in the east, west, north, and south regions, respectively for $k = 2, 3, 4$, and 5. We only display the southern sub-stencil \mathcal{S}_5 .

of cell averages $\mathbf{g}_{(k)}$ of $f(\mathbf{x})$ supported on the k^{th} (sub)stencil, GP-WENO-AO forms the reconstruction (see also Appendix A in [21])

$$\tilde{f}(\mathbf{x}^*) = \frac{\omega_0}{\gamma_0} \mathbf{r}_{(0)}^T \mathbf{g}_{(0)} + \sum_{k=1}^5 \left(\omega_k - \omega_0 \frac{\gamma_k}{\gamma_0} \right) \mathbf{r}_{(k)}^T \mathbf{g}_{(k)}, \quad (24)$$

where, following the conventional notations, γ_k and ω_k are the linear and normalized nonlinear weights, respectively. Note that if $\omega_k \rightarrow \gamma_k$ for all k in the absence of discontinuities on the highest order stencil \mathcal{S}_0 , the coefficient on the first term tends to one, and the term in parentheses tends to zero. Hence, when the nonlinear weights ω_k approach the linear weights γ_k , the highest accuracy GP reconstruction $\mathbf{r}_{(0)}^T \mathbf{g}_{(0)}$ is selected, and full accuracy can be maintained independently of how γ_k are chosen. Similar to [52], we fix $\gamma_{hi} = \gamma_{lo} = 0.8$, and set the linear weights as $\gamma_0 = \gamma_{hi}$ for \mathcal{S}_0 , $\gamma_1 = (1 - \gamma_{hi})\gamma_{lo}$ for \mathcal{S}_1 , and $\gamma_k = (1 - \gamma_{hi})(1 - \gamma_{lo})/4$ for the remaining biased substencils \mathcal{S}_k with $k = 2, \dots, 5$, in which case the sum of the linear weights satisfies $\sum_{k=0}^5 \gamma_k = 1$ as in [52]. We provide the explicit form of the nonlinear weights $\tilde{\omega}_k$ and ω_k in the next section.

3.3. Multidimensional smoothness indicators and nonlinear weights

The nonlinear weights, unnormalized $\tilde{\omega}_k$ and the associated normalized ω_k , and the smoothness indicators β_k within them, must be specified in an appropriate way for the reconstruction in Eq. (24) to simultaneously provide accurate reconstructions for smooth data and limited reconstructions for non-smooth data. In this section, we introduce new *multidimensional* smoothness indicators β_k on each \mathcal{S}_k for our GP-WENO-AO, which measure the relative smoothness of the reconstructed function \tilde{f}_k in Eq. (14) over each \mathcal{S}_k in a *multidimensional* way.

We construct these indicators β_k so that they approximate the square of a scaled H_2 semi-norm $|\tilde{f}_k|_{H^2}^2$, i.e., $\beta_k \approx |\tilde{f}_k|_{H^2}^2$, where we set

$$|\tilde{f}_k|_{H^2}^2 = \frac{1}{\Delta} \sum_{|\alpha|=1}^2 \int_{\Omega} \left(\Delta^{|\alpha|} \frac{\partial^{|\alpha|} \tilde{f}_k}{\partial \mathbf{x}^\alpha} \right)^2 dx = \sum_{|\alpha|=1}^2 \int_{\hat{\Omega}} \left(\frac{\partial^{|\alpha|} \tilde{f}_k}{\partial \hat{\mathbf{x}}^\alpha} \right)^2 d\hat{\mathbf{x}}. \quad (25)$$

Here, Ω is the central cell where reconstruction is being performed and α is a multi-index². Note that $\Delta^{|\alpha|}$ is present in the first formula to make the quantity in the parentheses independent of the grid-scale in the same conceptual manner the undivided differences do in standard polynomial WENO methods. This can easily be recast as integration over the unit square $\hat{\Omega}$ in the second formula by making the change of variables $\hat{\mathbf{x}} = \mathbf{x}/\Delta$, and defining the kernel with respect to ℓ/Δ as in Section 3.1. This is shown in the second part of Eq. (25) where this change of variables has conveniently removed all explicit dependence on the grid-scale Δ . We note that the same process holds when

²For our two-dimensional setting, we set $\mathbf{x} = (x_1, x_2)$ and $\alpha = (\alpha_1, \alpha_2)$, where each component α_i is a nonnegative integer and we follow the customary notation of writing $|\alpha| = \alpha_1 + \alpha_2$. For any differentiable function u , the α partial derivative in Eq. (26) is defined by $\partial^{|\alpha|} u / \partial \mathbf{x}^\alpha = \partial_{x_1}^{\alpha_1} \partial_{x_2}^{\alpha_2} u$ subject to each $|\alpha| = 1$ and $|\alpha| = 2$.

$\Delta x \neq \Delta y$, and there is no single grid-scale Δ due to the separable nature of the kernels considered herein. Experience has shown that using the H_2 semi-norm, and hence summing over partial derivatives with $|\alpha| \leq 2$, can sufficiently down-weight (sub)stencils containing discontinuities while managing the amount of computational expense. More partial derivatives could easily be incorporated at a greater computational expense.

The scaled H_2 semi-norm in the second part of Eq. (25) cannot be integrated in closed form and is to be integrated using a quadrature rule. To define β_k such that $\beta_k \approx |\widetilde{f}_k|_{H^2}^2$, we use a quadrature rule

$$\beta_k = \sum_{|\alpha|=1}^2 \sum_q w_q \left(\frac{\partial^{|\alpha|} \widetilde{f}_k}{\partial \hat{\mathbf{x}}^\alpha} \Big|_{\hat{\mathbf{x}}_q} \right)^2, \quad (26)$$

where $\hat{\mathbf{x}}_q$ are quadrature points from a 2×2 tensor-product Gauss-Legendre rule with associated weights w_q [53]. Using the reference integral region of $[0, 1] \times [0, 1]$, we adopt the values given as

$$\hat{\mathbf{x}}_q = \left(\frac{3 \pm \sqrt{3}}{6}, \frac{3 \pm \sqrt{3}}{6} \right), \quad w_q = \frac{1}{4}, \quad 1 \leq q \leq 4. \quad (27)$$

The calculation of $\frac{\partial^{|\alpha|} \widetilde{f}_k}{\partial \hat{\mathbf{x}}^\alpha} \Big|_{\hat{\mathbf{x}}_q}$ in Eq. (26) from cell-average data $\mathbf{g}^{(k)}$ on the k^{th} (sub)stencil proceeds in much the same way as the reconstruction of Riemann states along the boundary done in Eq. (14), except that we now need a differentiated version. Differentiating the kernel reconstruction in Eq. (9) yields

$$\frac{\partial^{|\alpha|} \widetilde{f}_k}{\partial \hat{\mathbf{x}}^\alpha} \Big|_{\hat{\mathbf{x}}_q} = \sum_{l=1}^N \alpha_l \lambda_l^{(\hat{y})} \frac{\partial^{|\alpha|} K(\hat{\mathbf{x}}, \hat{\mathbf{y}})}{\partial \hat{\mathbf{x}}^\alpha} \Big|_{\hat{\mathbf{x}}=\hat{\mathbf{x}}_q}, \quad (28)$$

hence a prediction vector for each partial derivative can be obtained from Eq. (15) where the sample vector \mathbf{T} is replaced by

$$[\mathbf{D}]_l = \lambda_l^{(\hat{y})} \frac{\partial^{|\alpha|} K(\hat{\mathbf{x}}, \hat{\mathbf{y}})}{\partial \hat{\mathbf{x}}^\alpha} \Big|_{\hat{\mathbf{x}}=\hat{\mathbf{x}}_q}, \quad (29)$$

giving $\frac{\partial^{|\alpha|} \widetilde{f}_k}{\partial \hat{\mathbf{x}}^\alpha} \Big|_{\hat{\mathbf{x}}_q} = \mathbf{D}^T \mathbf{C}^{-1} \mathbf{g}^{(k)}$ in total. A separate prediction vector is required for each $\hat{\mathbf{x}}_q$ and each α , resulting in 20 total prediction vectors to generate each β_k . We also have found that the mixed partial derivative $\partial^2 / \partial x_1 \partial x_2$ does not contribute substantially to the smoothness indicators and can safely be removed to reduce the computational cost of constructing each β_k . In this case, only four out of the total five partial derivatives are utilized, i.e., $\partial / \partial x_1$, $\partial / \partial x_2$, $\partial^2 / \partial x_1^2$, $\partial^2 / \partial x_2^2$ but excluding $\partial^2 / \partial x_1 \partial x_2$, reducing the number of needed prediction vectors from 20 to 16, in combination with the four quadrature points, $\hat{\mathbf{x}}_q$, $q = 1, \dots, 4$ for Eq. (26).

Finally, the nonlinear weights ω_k are generated from the smoothness indicators β_k through a slightly modified version of the WENO-Z weights [54, 55]. The unnormalized weights for each stencil are calculated as

$$\widetilde{\omega}_k = \gamma_k \left(1 + \left(\frac{\tau}{\beta_k + \epsilon} \right)^p \right), \quad (30)$$

where we set $\epsilon = \left(\frac{2\Delta x\Delta y}{\Delta x + \Delta y}\right)^{R-1}$ and the exponent is set equal to the stencil radius $p = R$. The global smoothness indicator τ is defined as

$$\tau = \left| \beta_0 - \frac{1}{4} \sum_{l=2}^5 \beta_l \right|. \quad (31)$$

Note that as in WENO-Z [54, 55] the smoothness indicator for the central substencil, β_1 , is not used in the calculation of τ . The form of ϵ was chosen experimentally, though was guided by the observation that τ should be $\mathcal{O}(\Delta^{R-1})$ for smooth data. Finally, the unnormalized nonlinear weights $\widetilde{\omega}_k$ are normalized to obtain the so-called normalized weights as

$$\omega_k = \frac{\widetilde{\omega}_k}{\sum_k \widetilde{\omega}_k}. \quad (32)$$

With ω_k , Eq. (24) is now applied to find each of the Riemann states in turn.

3.4. Variables for reconstruction

The multidimensional WENO reconstruction procedure detailed in the prior subsections is defined for scalar fields, thus reconstructing the Riemann states requires that the cell average states be separated into scalar fields. It is well known that performing reconstruction directly on the conservative variables leads to oscillatory results in the vicinity of shocks. As such, the cell averages of the conservative variables throughout the stencil need to be converted to another form prior to reconstruction.

Generically, for a system of N conservation laws, one can fix a transformation matrix Φ of size $N \times N$. Denoting a vector of the local cell-averaged conservative variables at each cell (x_i, y_j) by $U_{i,j}$, a conversion from $U_{i,j}$ to a choice of the reconstruction variable $W_{i,j}$ is done by

$$W_{i,j} = \Phi U_{i,j}, \quad \forall i, j \in \mathcal{S}_0. \quad (33)$$

Reconstruction then proceeds over W component-wise yielding a pointwise estimate of each component w_* of W , from which each pointwise conservative component of the Riemann state u_* can be obtained as

$$u_* = \Phi^{-1} w_*. \quad (34)$$

Crucially, Φ must be constant throughout the stencil for the accuracy of the reconstruction to be maintained. In the following two subsections, we describe two ways to choose the transformation matrix Φ . Section 3.4.1 briefly overviews the most popular choice with characteristic variables, which is computationally expensive. In Section 3.4.2, we address this issue by introducing a new approach using so-called *linearized primitive* variables.

3.4.1. Characteristic variables

It is widely known in the computational fluid dynamics community that the best results come from reconstruction in characteristic variables. For each fixed direction η

and reference state $\tilde{\mathbf{U}}$ ³, the flux Jacobian

$$\mathbf{A} = \left. \frac{\partial \mathbf{F}_\eta}{\partial \mathbf{U}} \right|_{\tilde{\mathbf{U}}} \quad (35)$$

is evaluated from the η directional flux \mathbf{F}_η . Then the eigendecomposition $\mathbf{A} = \mathbf{R}\mathbf{\Lambda}\mathbf{L}$ is computed, and the transformation matrix is set as $\mathbf{\Phi} = \mathbf{L}$ with $\mathbf{\Phi}^{-1} = \mathbf{R}$. The reference state $\tilde{\mathbf{U}}$ is chosen as the cell average in the central cell of the stencil. Note that since the eigenvectors of the flux Jacobian depend nonlinearly on the components of the reference state $\tilde{\mathbf{U}}$, this only provides a second-order accurate approximation of the wave structure within the central cell; however, the limited accuracy of the wave structure estimation does not influence the mathematical property of the reconstruction accuracy.

3.4.2. Linearized primitive variables

A critical drawback to using characteristic variables is that the nonlinear weights within the WENO reconstruction must be re-calculated when the direction η is changed. On structured two-dimensional grids, these nonlinear weights need to be calculated twice for each cell, once in the x -direction for the reconstruction of the $(i \pm 1/2, j)$ Riemann states, and again in the y -direction for the $(i, j \pm 1/2)$ Riemann states. The situation worsens further for unstructured grids, with the nonlinear weights being re-evaluated for each and every face of the cell.

A cost-effective alternative can be made available with primitive variables that provide much better reconstruction than conservative variables in the vicinity of shocks with fewer oscillations. They are more computationally friendly than characteristic variables by being direction-independent, hence needing half as many nonlinear weight calculations (with even greater savings on unstructured grids). Of course, the primitive variables depend nonlinearly on the conservative variables; hence converting all conservative variables in the stencil to primitive variables *naively* will reduce the accuracy to second-order immediately and irreversibly. To address this, we introduce a new approach below.

Let \mathbf{V} denote the primitive variables, and again set $\tilde{\mathbf{U}}$ as a reference state in conservative variables. The reduction to second-order accuracy can be ameliorated by linearizing the map from conservative to primitive variables around the reference state as

$$\mathbf{V}(\mathbf{U}) \approx \mathbf{V}(\tilde{\mathbf{U}}) + \left. \frac{\partial \mathbf{V}}{\partial \mathbf{U}} \right|_{\tilde{\mathbf{U}}} (\mathbf{U} - \tilde{\mathbf{U}}) = \left. \frac{\partial \mathbf{V}}{\partial \mathbf{U}} \right|_{\tilde{\mathbf{U}}} \mathbf{U} + \left(\mathbf{V}(\tilde{\mathbf{U}}) - \left. \frac{\partial \mathbf{V}}{\partial \mathbf{U}} \right|_{\tilde{\mathbf{U}}} \tilde{\mathbf{U}} \right). \quad (36)$$

This can be applied over the entire stencil to generate approximate cell average values of the primitive variables *relative* to $\tilde{\mathbf{U}}$. Just as the limited accuracy of the wave structure in the characteristic variables approach does not affect the overall accuracy of the reconstruction, the limited accuracy of this linearization has no bearing on the accuracy of the overall reconstruction.

³The reference state $\tilde{\mathbf{U}}$ is the vector of cell-averaged conservative values at the central cell of the full stencil \mathcal{S}_0 depicted with the solid diamond in Fig. 1 and Fig. 2, where the reconstruction is performed.

The constant part of this expression, $(\mathbf{V}(\bar{U}) - \frac{\partial \mathbf{V}}{\partial \bar{U}}|_{\bar{U}} \bar{U})$, has no influence on the nonlinear weights since it will disappear due to the derivatives in Eq. (26). Dropping the constant part, we establish the conversion relation Eq. (33) in the form of

$$\mathbf{W} \equiv \mathbf{V}(\mathbf{U}) \approx \frac{\partial \mathbf{V}}{\partial \mathbf{U}} \Big|_{\bar{U}} \mathbf{U} \equiv \mathbf{\Phi} \mathbf{U}, \quad (37)$$

where, for the purposes of reconstruction, we simply set

$$\mathbf{\Phi} = \frac{\partial \mathbf{V}}{\partial \mathbf{U}} \Big|_{\bar{U}}. \quad (38)$$

Eq. (37) is our new rule for the two-way conversion in Eq. (33) and Eq. (34). This has the added benefit of requiring approximately half as many operations as the characteristic variable case. Additionally, the similarity in how these reconstruction variables are produced compared to the characteristic variables makes it straightforward to support both options within a single code base. We also note that finding $\mathbf{\Phi}$ and $\mathbf{\Phi}^{-1}$ is substantially simpler than finding the eigendecomposition of the flux Jacobian. As such, this approach may be interesting for more complicated systems of conservation laws, e.g., Euler equations with complicated equations of state, multi-fluid equations, and magnetohydrodynamics equations, to name a few.

4. Positivity preservation

The WENO method discussed in Section 3 is adequate for many shock problems. However, problems exhibiting very strong shocks or near vacuum states may encounter negative states in the density and/or pressure variables during evolution. The high Mach number astrophysical jets [56, 57, 25] shown in Section 6.6 are one such example.

To ameliorate issues with negativity, the above method can be combined with a modified version of the positivity-preserving limiter introduced in [57], which itself is similar to the methods described in [58, 59]. We note that, while the method presented here is not provably positivity-preserving, it is straightforward to implement and has not yet been observed to fail in practical applications. The innovation in [57] is the selection of density and pressure bounds in a data-dependent manner that reduces the impact of extra parameters needing problem-specific tuning.

The current method only differs from [57] in that only the Riemann states are considered, and no reconstructions are done in the interior of the cell to test for positivity there. A full description will be given here for completeness. In what follows let the index s label the individual quadrature points on the faces of the cell (i, j) , such that \mathbf{u}_s would be the pointwise reconstructed Riemann state at quadrature point s , and $\mathbf{U}_{i,j}$ would be the cell average. Note that the single index s runs over the quadrature points on all four faces of the cell.

4.1. Density and pressure bounds

The limiter does not enforce *a-priori* chosen bounds on the density and pressure, e.g., no hard-setting of floor and/or ceiling values. Instead, these bounds are chosen in a way dependent on the local flow conditions around the cell where limiting is being

performed. The density of each Riemann state is constrained from above and below such that $\rho_s \in [\rho_{min}, \rho_{max}]$ with $\rho_{min} > 0$, while the pressure is constrained only from below such that $p_s \geq p_{min} > 0$. These bounds depend upon the local cell average densities and pressures,

$$\rho_{max} = \tilde{\rho}_{max} (1 + \kappa_2 - \kappa_2 \eta), \quad \tilde{\rho}_{max} = \max_{-1 \leq i, j \leq 1} \{\rho_{i,j}\}, \quad (39)$$

$$\rho_{min} = \tilde{\rho}_{min} (1 - \kappa_2 + \kappa_2 \eta), \quad \tilde{\rho}_{min} = \min_{-1 \leq i, j \leq 1} \{\rho_{i,j}\}, \quad (40)$$

$$p_{min} = \tilde{p}_{min} (1 - \kappa_2 + \kappa_2 \eta), \quad \tilde{p}_{min} = \min_{-1 \leq i, j \leq 1} \{p_{i,j}\}, \quad (41)$$

where η adjusts how strict the bounds are by tending to unity only in compressive regions. As in [57], we find no compelling reason to enforce a maximum value for the pressure, and we do not utilize p_{max} henceforth. The flattener η is defined by

$$\eta = \min \left\{ 1, \max \left\{ 0, -\frac{\kappa_1 \tilde{a}_{min} + \nabla \cdot \mathbf{v}}{\kappa_1 \tilde{a}_{min}} \right\} \right\}, \quad (42)$$

where $\tilde{a}_{min} = \min_{-1 \leq i, j \leq 1} \{a_{i,j}\}$ is the minimum local sound speed in the neighboring cells. Herein, the constants κ_1 and κ_2 are both set to 3/10. While these constants are independent of the local data, they do not seem to need any problem-specific tuning. Note that the pressures and the sound speeds used throughout this section are calculated directly using cell average values rather than pointwise values and are hence only second-order accurate.

4.2. Application of the limiter

With the allowable bounds on density and pressure known, the Riemann states on the boundary of each cell are modified by the positivity-preserving limiter in two stages. The limiter first ensures that the density is bounded above and below such that $\rho_s \in [\rho_{min}, \rho_{max}]$. The size of the needed correction is given by

$$\theta_\rho = \min_s \left\{ 1, \frac{\rho_{i,j} - \rho_{min}}{\rho_{i,j} - \rho_s}, \frac{\rho_{max} - \rho_{i,j}}{\rho_s - \rho_{i,j}} \right\}, \quad (43)$$

and the Riemann states are corrected via

$$\mathbf{u}_s \leftarrow \mathbf{U}_{i,j} + \theta_\rho (\mathbf{u}_s - \mathbf{U}_{i,j}). \quad (44)$$

There are two important observations to make here. First, all components of all Riemann states are modified in the same way to ensure consistency, and second, there will be no modification to the states if all densities lie in the desired range to begin with.

All Riemann states will now have valid densities, but the pressures may not yet be bounded below by p_{min} . As discussed in [57, 58, 59], the convexity of the physically admissible region allows this minimum pressure to be enforced again by rewriting the states as a convex combination of their current values and the cell average value $\mathbf{U}_{i,j}$. That is to say,

$$\mathbf{u}_s \leftarrow \mathbf{U}_{i,j} + \theta_p (\mathbf{u}_s - \mathbf{U}_{i,j}), \quad (45)$$

though now the selection of θ_p is slightly more elaborate than that of θ_ρ . In this case, the required correction for a particular s appears as the root of the quadratic equation

$$\begin{aligned} & \theta_{p,s}^2 \left(2(\rho_s - \rho_{i,j})(E_s - E_{i,j}) - \|\mathbf{m}_s - \mathbf{m}_{i,j}\|^2 \right) + \\ & \theta_{p,s} \left(2\rho_{i,j}(E_s - E_{i,j}) + 2E_{i,j}(\rho_s - \rho_{i,j}) - 2(\mathbf{m}_s - \mathbf{m}_{i,j}) \cdot \mathbf{m}_{i,j} - 2e_{min}(\rho_s - \rho_{i,j}) \right) + \\ & \left(2\rho_{i,j}(E_{i,j} - e_{min}) - \|\mathbf{m}_{i,j}\|^2 \right) = 0, \end{aligned} \quad (46)$$

where $\mathbf{m} = \rho\mathbf{u}$ is the fluid momentum and $e_{min} = p_{min}/(\gamma - 1)$ is the internal energy associated to the minimum pressure. The smallest admissible root $\theta_p = \min\{\theta_{p,s} \mid 0 \leq \theta_{p,s} \leq 1\}$ is chosen. As before, it should be noted that all components of all Riemann states are modified in unison, and no correction will be applied if all pressures appearing in the Riemann states already satisfy $p_s \geq p_{min}$. Additionally, this correction naturally leaves the densities bounded appropriately.

5. Step-by-step procedures of the GP-WENO FVM in 2D

All of the building blocks of the proposed scheme have now been defined. Now, we gather them together into an explicit step-by-step description. The application of the solver proceeds in three main stages, where the first and the second stages are conducted one-time as part of the initial setup, after which the last stage is performed repeatedly to evolve solutions until the final simulation time. They include (i) constructing the stencils and weight vectors, (ii) evaluating initial conditions into cell averages, and finally, (iii) advancing the cell averages through time. We elaborate on each of these stages in the following subsections.

5.1. Construction of stencils and weight vectors

To prepare the stencils for use in each uniform grid simulation, one needs to:

1. Enumerate all cells in the full stencil, \mathcal{S}_0 , and the remaining substencils, \mathcal{S}_k , $k = 1, \dots, 5$.
2. Construct prediction vectors, $\mathbf{r}^{(k)}$, $k \geq 0$ in Eq. (15), for each face quadrature point \mathbf{x}^* relative to each (sub)stencil using Eq. (14). We set the number of quadrature points used on each face using an $R + 1$ point Gauss-Legendre quadrature rule. This guarantees the $2(R + 1)^{\text{th}}$ accuracy to ensure that the resulting calculation of the face-averaged fluxes does not limit the $(2R + 1)^{\text{th}}$ reconstruction accuracy of the GP-WENO scheme.
3. Construct prediction vectors for all partial derivatives needed to evaluate Eq. (26) relative to each (sub)stencil.

We note that the matrix in Eq. (12) is ill-conditioned for large values of the hyperparameter ℓ relative to the grid resolution Δ , in which case the construction of the prediction vectors $\mathbf{r}^{(k)}$ requires care. However, since this process only needs to be carried out once

in the setup phase for each uniform grid simulation, one is free to use more expensive (e.g., quadruple precision in [20, 21, 25]) and stable inversion schemes. As described in Section 2.3, we use the Contour-Padé method from [46] as the choice of our stable inversion scheme in this study.

5.2. Evaluation of initial conditions into cell averages

A high-accuracy evaluation of the initial conditions is straightforward, although it is necessary for achieving the target rates of convergence in finite volume numerical solutions. To do this, the initial cell averages must be filled to an appropriate level of accuracy using an appropriate quadrature rule. The simplest way is through a tensor-product Gauss-Legendre rule on each cell. To this end, we adopt the 10th order accurate 5-point Gauss-Legendre rule per dimension for initialization to guarantee that the initial condition is set to higher accuracy than the remaining operations in the simulation. The same rule was adopted in our earlier study [25] as well.

5.3. Advancement of GP-WENO through time

We describe the overall solution advancement of the GP-WENO solver whose high-order spatial solutions are temporally evolved by multistage Runge-Kutta (RK) type integrators⁴. In order for our GP-WENO solutions to achieve the target high-order accuracy (e.g., the 5th, 7th, and 9th convergence rates in this study), we need to find such high-order *face-averaged* fluxes within each stage of the RK integrator. The overall path to these face-averaged fluxes is standard across many finite volume schemes, which proceeds in five steps as below:

1. Fill ghost cells in accordance with the boundary conditions.
2. Calculate Riemann states at each quadrature point on cell faces. This step is divided into the following six sub-steps:
 - Gather cell-average states from all cell centers in the full stencil \mathcal{S}_0 .
 - Construct transformation matrix Φ in Eq. (38) using the central cell data $\tilde{\mathbf{U}}$ (e.g., the conservative variables in the solid diamond cell in Figs. 1 and 2) as the reference state.
 - For each $(i, j) \in \mathcal{S}_0$, project all conservative cell average data $U_{i,j}$ to the corresponding linearized primitive variables $\mathbf{W}_{i,j}$, according to Eq. (33).
 - For each k , $0 \leq k \leq 5$, the linearized 2D variables $\mathbf{W}_{i,j}$ are now enumerated (in a consistent fashion) and are cast into the associated long 1D data arrays, $\mathbf{g}^{(k)}$.
 - Using all the calculated 1D linearized primitive data $\mathbf{g}^{(k)}$, $0 \leq k \leq 5$, from all cells $(i, j) \in \mathcal{S}_0$ reconstruct the high-order pointwise, componentwise values \mathbf{w} in linearized primitive variables at all face quadrature points \mathbf{x}^* via the GP-WENO-AO reconstruction in Eq. (24).

⁴The choice of RK integrators are explicitly specified in Section 6.

- At all cell face quadrature points \mathbf{x}^* , project the reconstructed pointwise linearized primitive values \mathbf{w} back to conservative variables \mathbf{u} to maintain high-order accuracy according to the conversion rule in Eq. (34).
 - Apply the positivity preserving limiter, following the strategies in Section 4, to the reconstructed high-order conservative Riemann state variables \mathbf{u} at all quadrature points.
3. Populate Riemann states outside of the physical domain in accordance with the boundary conditions using ghost cell filling.
 4. Call Riemann solver at each flux quadrature point.
 5. Integrate fluxes and update cell averages in accordance with the chosen RK method.

Naturally, the second step of calculating the high-order GP-WENO-AO Riemann states contains most of the contributions from this work.

6. Numerical Results

The presented scheme is evaluated against a variety of challenging and standard benchmark problems. While Section 3.4.2 and Section 4 are specific to the compressible Euler equations, the overall GP scheme can be applied to solving more generic governing systems. To this end, we begin this section by first demonstrating the solver on the Smolarkiewicz linear advection problem [60]. Then, before going to fully two dimensional problems we solve the Sod shock tube problem [61] in grid aligned and tilted configurations in a two-dimensional domain. Next, we study the accuracy of our scheme evaluated against the nonlinear isentropic vortex problem [62]. Moving on to shock-dominant problems, we demonstrate challenges regarding symmetry preservation through the third configuration 2D Riemann problem [63]. Our scheme is further tested on a shock-density interaction problem [64] that leads to the Richtmeyer-Meshkov instability. Finally, the positivity preservation capabilities of the scheme are stressed through a pair of high Mach astrophysical jet benchmarks [57, 25].

All problems are advanced in time using the five-stage fourth-order RK-SSP(5,4) method [65, 66] under a CFL number of 0.75, except for the isentropic vortex, which uses an 11-stage 7th-order RK(11,7) [30]. This time integrator is sufficiently accurate for the experimental convergence rates in the isentropic vortex problem to be dominated by spatial errors for all considered resolutions. All problems with the Euler equations utilize the HLLC Riemann solver. For reconstruction, the new linearized primitive reconstruction in Section 3.4.2 is the default choice in all Euler benchmarks, with the exception of the third configuration Riemann problem, which uses characteristic reconstruction. The positivity preserving limiter of Section 4 is enabled for all Euler problems but our observations show that the limiter is rarely gets applied apart from the astrophysical jet problems. The number of quadrature points used on each face is always set as $R + 1$, yielding $2(R + 1)$ th accuracy, to ensure that the calculation of the face-averaged fluxes does not limit the accuracy of the scheme. Finally, the length scale used in the definition of the kernel function is set to $\ell = 12\Delta x$ unless otherwise noted.

6.1. Smolarkiewicz advection

The Smolarkiewicz deformational flow problem [60] tracks the advection of a passive scalar in a solenoidal velocity field. The governing equation is

$$\frac{\partial u}{\partial t} + \nabla \cdot (\mathbf{v}u) = 0, \quad (47)$$

where the fixed velocity field satisfying $\nabla \cdot \mathbf{v} = 0$ describes a collection of counter-rotating vortices given by

$$\mathbf{v} = 8k \begin{pmatrix} \sin(kx) \sin(ky) \\ \cos(kx) \cos(ky) \end{pmatrix}, \quad k = \frac{2\pi}{50}. \quad (48)$$

The problem is configured on the domain $\Omega = [0, 100] \times [0, 100]$ with periodic boundary conditions at all boundaries. The passive scalar u is initially distributed in a circle of radius 15 in the center of the domain. Specifically

$$u(x, y, 0) = \max \left\{ 1 - \frac{r}{15}, 0 \right\}, \quad r^2 = (x - 50)^2 + (y - 50)^2, \quad (49)$$

which is chosen such that its support overlaps six of the vortices.

This test provides a useful, though qualitative, measure of the artificial dissipation inherent to the method. As the initial condition is supported on only six of the vortices, the exact solution outside of these vortices should remain zero for all time. Any leakage out of these vortices is directly attributable to artificial dissipation.

Fig. 4 shows the solutions obtained from the presented methods at a final time of $t_{\max} = 263.76$, at resolutions of 100×100 and 200×200 using stencils with radii $R = 2$ and 3. The final time was chosen to allow comparison with the results presented in [43]. We observe that there is minimal leakage out of the central six vortices, and that qualitatively the proposed methods have little numerical dissipation.

6.2. Sod shock tube

The Sod shock tube [61] is a classic benchmark problem in 1D for assessing numerical schemes for the compressible Euler equations. Here we solve this problem in grid-aligned and grid-tilted configurations on 2D domains.

The initial data for this problem is piecewise constant, where the left and right states are

$$(\rho_L, u_L, v_L, P_L) = (1, 0, 0, 1) \quad (50)$$

$$(\rho_R, u_R, v_R, P_R) = (0.125, 0, 0, 0.1). \quad (51)$$

The grid-aligned version of the problem is solved on the domain $\Omega = [0, 1] \times [0, 0.04]$ with outflow boundary conditions and is initialized to the left state for $x < 0.5$, and the right state otherwise. The setup for the tilted problem follows [67], and is solved on the domain $\Omega = [0, \sqrt{5}] \times [0, 2\sqrt{5}]$ with periodic boundary conditions. The initial data is organized with respect to the transformed coordinate, $x_{\parallel} = x \cos \alpha + y \sin \alpha$,

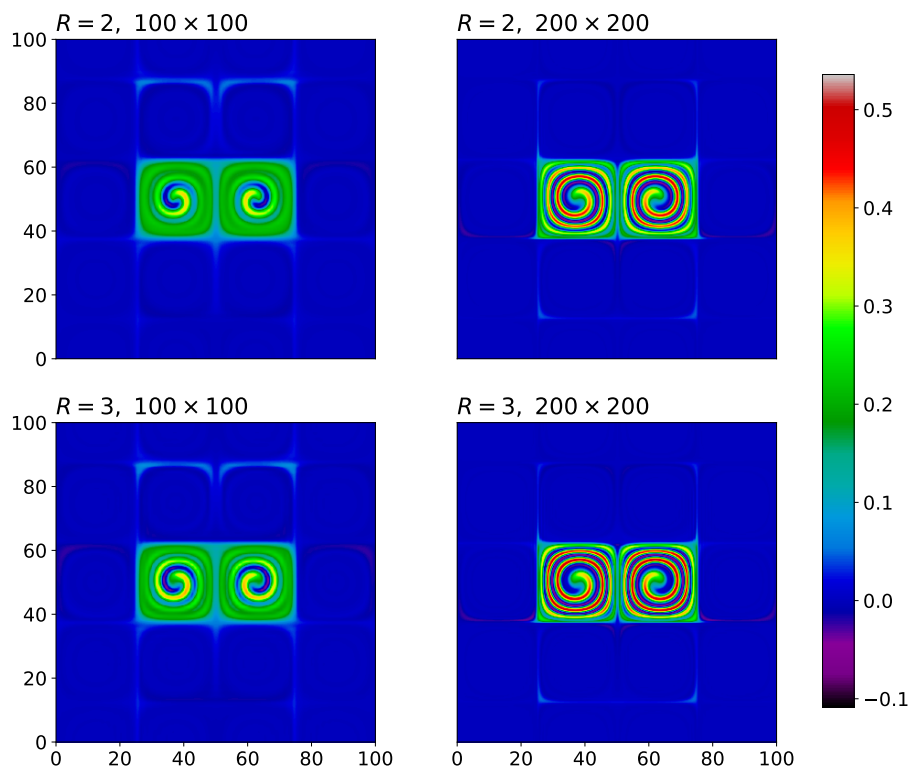


Figure 4: The solution of the Smolarkiewicz advection problem is shown at the final time $t_{\max} = 263.76$ with grid resolutions of 100×100 and 200×200 , and stencil radii of $R = 2$ and 3 .

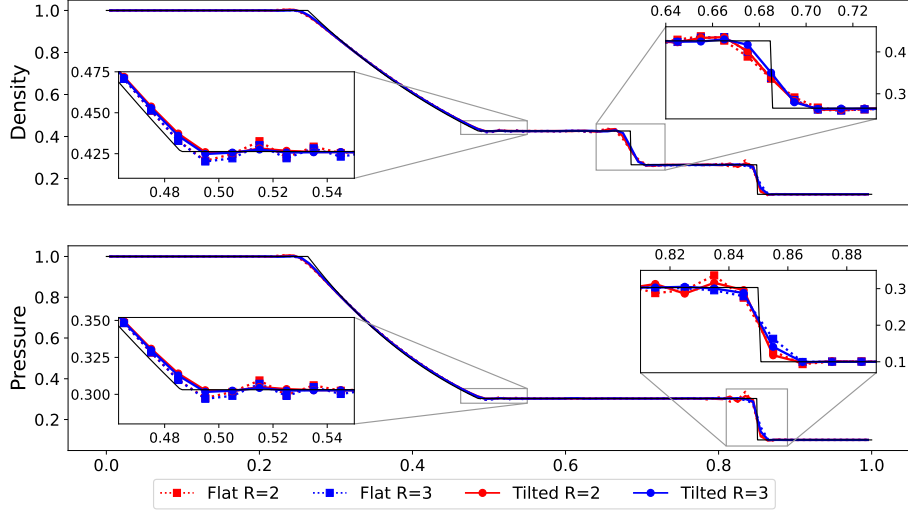


Figure 5: Slices of the density and pressure for the Sod shock tube problem are shown for both the grid-aligned and the grid-tilted configurations. The grid-aligned cases have 100 cells in the x -direction, and are shown as dotted lines. Traces from the tilted configurations have an equivalent resolution and are shown as solid lines. Red lines correspond to results obtained using stencils of radius $R = 2$, and blue lines correspond to results obtained using stencils of radius $R = 3$. The exact solution is shown as a solid black line. Within the insets, the flat and tilted configurations are further distinguished by square and circular markers, respectively.

where $\alpha = \tan^{-1}(0.5) \approx 26^\circ$. The left state is initially applied in the region $\mathcal{R} = \cup_{k=1}^3 \mathcal{R}_k$ consisting of three stripe regions, $\mathcal{R}_k, k = 1, 2, 3$, which are defined by

$$\mathcal{R}_1 = \{(x, y) : x_{\parallel} < 0.5\}, \quad \mathcal{R}_2 = \{(x, y) : 1.5 < x_{\parallel} < 2.5\}, \quad \mathcal{R}_3 = \{(x, y) : x_{\parallel} > 3.5\}. \quad (52)$$

The right state initializes the rest of the domain apart from the region \mathcal{R} .

Fig. 5 compares slices of the density and pressure for the grid-aligned and grid-tilted configurations at the final time of $t_{\max} = 0.2$, using stencils of radii 2 and 3. The grid-aligned cases use a grid resolution of 100×4 . The tilted cases use an equivalent resolution of 250×1000 , which notably produces non-square cells. The solutions in all cases are comparable to the exact solution, showing that the proposed scheme does not strongly favor grid-aligned phenomena over unaligned phenomena.

6.3. Isentropic vortex

As is now standard, we use the isentropic vortex problem to validate the nonlinear accuracy of our proposed method for smooth solutions. Following [68], the problem is posed on $\Omega = [-10, 10]^2$ with periodic boundary conditions, and initial condition is set as

$$\begin{pmatrix} \rho \\ u \\ v \\ P \end{pmatrix} = \begin{pmatrix} \left(1 + \frac{1}{2}(1 - \gamma)\omega^2\right)^{\frac{1}{\gamma-1}} \\ 1 - \omega y \\ 1 + \omega x \\ \gamma^{-1} \left(1 + \frac{1}{2}(1 - \gamma)\omega^2\right)^{\frac{\gamma}{\gamma-1}} \end{pmatrix}, \quad (53)$$

Table 1: The errors and experimental orders of convergence (EOC) measured in the L_1 and L_∞ norms are gathered here for the density in the isentropic vortex problem. The squared exponential kernel in Eq. (16) is used throughout, and the hyperparameter is fixed at $\ell = 2$ for all resolutions, which translates to $\ell = 5\Delta x, 10\Delta x, 20\Delta x,$ and $40\Delta x$ in grid units.

Grid	L_1 Error	L_1 Order	L_∞ Error	L_∞ Order
$R = 2$				
50^2	$1.43e - 1$	–	$2.29e - 2$	–
100^2	$1.49e - 2$	3.27	$4.49e - 3$	2.35
200^2	$6.20e - 4$	4.58	$9.52e - 5$	5.56
400^2	$2.04e - 5$	4.93	$3.24e - 6$	4.88
$R = 3$				
50^2	$8.37e - 2$	–	$1.89e - 2$	–
100^2	$2.36e - 3$	5.15	$3.13e - 4$	5.91
200^2	$3.18e - 5$	6.21	$1.06e - 5$	4.89
400^2	$2.72e - 7$	6.87	$9.58e - 8$	6.78
$R = 4$				
50^2	$4.42e - 2$	–	$9.31e - 3$	–
100^2	$6.94e - 4$	5.99	$2.34e - 4$	5.31
200^2	$2.53e - 6$	8.10	$1.11e - 6$	7.72
400^2	$5.70e - 9$	8.80	$2.30e - 9$	8.92
WENO-Z7				
50^2	$1.83e - 1$	–	$1.73e - 2$	–
100^2	$1.02e - 2$	4.17	$2.16e - 3$	3.00
200^2	$6.84e - 5$	7.22	$1.96e - 5$	6.79
400^2	$3.34e - 7$	7.68	$9.04e - 8$	7.76

where $\omega = \frac{5\sqrt{2}e}{4\pi}e^{-(x^2+y^2)/2}$. This setup describes an isentropic vortex traveling on a constant diagonal background velocity field. At the final time $t_{\max} = 20$ the vortex returns to its initial position, and the error accrued can be measured by comparing the initial and final states.

This problem is solved using stencils of radii $R = 2, 3,$ and $4,$ as well as the modified dimension-by-dimension 7th-order polynomial-based WENO-Z7 method from [30] for comparison. All reconstruction is done in the linearized primitive variables discussed in Section 3.4.2. The fluxes are calculated using $R+1$ Gauss-Legendre points on each face for the GP runs, thus yielding the $2(R+1)$ th-order accurate flux integrals for GP. The 7th-order WENO-Z7 method uses four points per face, providing the 8th-order accurate flux integrals. The cell averages at time $t = 0$ are populated by numerically integrating the initial condition in Eq. (53) with a 5-point tensor product Gauss-Legendre rule [53], the same approach we took in [25]. Time integration is performed using an 11-stage 7th-order RK7 method as in [30], which allows us to focus primarily on spatial errors up to the 7th-order GP runs with $R \leq 3$ in a theoretical sense.

Table 1 gathers the L_1 and L_∞ errors and experimental orders of convergence (EOC)

for the considered schemes. We measure the EOC as

$$\text{EOC} = \frac{\ln(E_c/E_r)}{\ln(2)}, \quad (54)$$

where E_c and E_r are the errors in the corresponding norm on the coarse and the next coarse resolutions (e.g., E_c on 50×50 and E_r on 100×100), respectively. First, we note that all schemes converge roughly at the desired order, including the 9th-order GP case with $R = 4$ even without any time step Δt reduction to match the lower 7th-order temporal accuracy of the chosen time integration scheme with the higher 9th-order spatial accuracy. The error remains spatially dominated for the considered resolutions. Furthermore, the error is already small enough that round-off and finite precision effects will likely dominate before the temporal error ever substantially contributes.

The kernel-based schemes presented in this paper approach their designed asymptotic orders of accuracy particularly closely as the grid is refined. As an aside, the WENO-Z7 method adapted from [30] exhibits an order of accuracy greater than designed and reported therein. This is likely due to our use of a larger domain size as discussed in [68].

6.4. 2D Riemann problem, configuration 3

The two-dimensional Riemann problems cataloged in [63] have become mainstays as benchmarks for schemes solving the compressible Euler equations. Here we solve the third configuration Riemann problem, which describes the interaction of four shock waves on the domain $\Omega = [0, 1] \times [0, 1]$. Outflow conditions are set on all boundaries, and the initial conditions, taken from [69], are

$$(\rho, \quad u, \quad v, \quad P) = \begin{cases} \left(\frac{77}{558}, \quad \frac{4}{\sqrt{11}}, \quad \frac{4}{\sqrt{11}}, \quad \frac{9}{310} \right), & x < 0.8, \quad y < 0.8, \\ \left(\frac{33}{62}, \quad 0, \quad \frac{4}{\sqrt{11}}, \quad \frac{3}{10} \right), & x > 0.8, \quad y < 0.8, \\ \left(\frac{33}{62}, \quad \frac{4}{\sqrt{11}}, \quad 0, \quad \frac{3}{10} \right), & x < 0.8, \quad y > 0.8, \\ \left(\frac{3}{2}, \quad 0, \quad 0, \quad \frac{3}{2} \right), & x > 0.8, \quad y > 0.8, \end{cases} \quad (55)$$

which slightly differ from those given in [63] in that they satisfy the Rankine-Hugoniot conditions more precisely.

As noted in [69], the solution to this problem should remain symmetric across the northeast and southwest diagonal for all time, but schemes with particularly low artificial dissipation are prone to breaking that symmetry. This is due to the accumulation of systematic rounding errors, and in particular, due to the errors in the non-associativity of floating point addition. The present implementation includes several of the fixes advocated for in the study reported in [69]. However, that study only considers dimension-by-dimension polynomial-based schemes, and the fully multidimensional scheme presented herein introduces several new concerns, which we discuss below further.

Fig. 6 and Fig. 7 show solutions to this problem under a variety of solver parameters. All such solutions maintain symmetry exactly. As in [69], we ensure that all summations over physically distinct quantities are computed in an associativity-agnostic fashion. Regardless, the multidimensional nature of the proposed scheme introduces

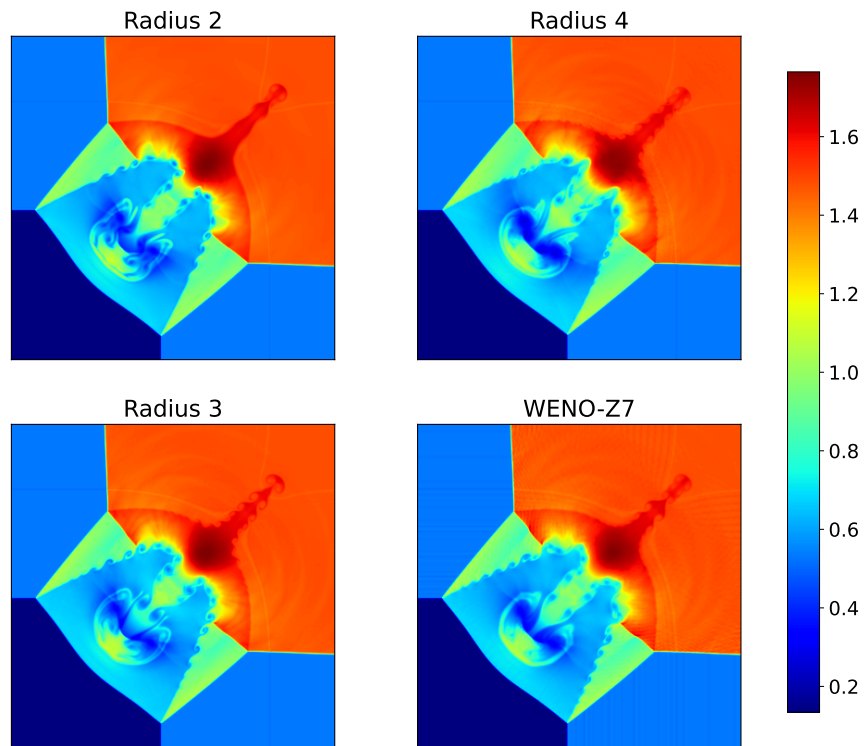


Figure 6: The density is shown at the final time $t_{\max} = 0.8$ for the third configuration 2D Riemann problem at stencil radii $R = 2, 3,$ and 4 on a 400×400 grid using the inverse quadratic kernel function in Eq. (17) with $\ell = 24\Delta x$. The lower right panel shows the solution obtained using WENO-Z7 in a dimension-by-dimension formulation with transverse corrections applied.

additional avenues for the accumulation of systematic associativity errors. We find that particular attention needs to be paid to the computation of the smoothness indicators defined in Eq. (26), and used in Eq. (30) and Eq. (31). When a stencil is mirrored across the diagonal, the north and east substencils (e.g., \mathcal{S}_4 and \mathcal{S}_2 in Fig. 1 and Fig. 2, respectively) swap their contents and roles, as do the south and west substencils (e.g., \mathcal{S}_5 and \mathcal{S}_3 in Fig. 1 and Fig. 2, respectively). To ameliorate these issues, we utilize pairwise summation wherever possible. For instance, the calculation of the global smoothness indicator τ in Eq. (31) is performed as

$$\tau = \left| \beta_0 - \frac{(\beta_2 + \beta_3) + (\beta_4 + \beta_5)}{4} \right|. \quad (56)$$

These fixes necessitate that the smoothness indicators β_k 's are calculated once for reconstruction on the north and south faces of each cell, and again for reconstruction on the east and west faces. These repeated calculations are precisely the same ones used when reconstruction is carried out in characteristic variables. These variables also allow for the longitudinal direction to be treated separately which avoids another source of associativity error. In principle this fix could be applied to the linearized primitive variables, but it's utility is so limited that we see no compelling reason to do so.

Additionally, the multidimensional nature of the (sub)stencils requires that the terms within the dot products $\mathbf{r}_{(k)}^T \mathbf{g}_{(k)}$, arising in Eq. (24) for instance, are accumulated in an associativity-agnostic fashion. We can control such dot products through the shape of the stencil and discrete symmetries of interest. We refer the interested reader to our implementation for further details and remark that the preservation of symmetry within multidimensional reconstruction schemes requires a much deeper investigation than the conventional dimension-by-dimension approach, which lies beyond the scope of the present study.

Fig. 6 compares the densities obtained from the presented scheme using the inverse quadratic kernel in Eq. (17) with different stencil radii against the dimension-by-dimension polynomial-based WENO-Z7 scheme. Each $(2R + 1)^{\text{th}}$ order accurate GP scheme with a radius R uses $R + 1$ Gaussian quadrature points for the $2(R + 1)^{\text{th}}$ order integration of the fluxes, while the WENO-Z7 method uses four points (hence yielding the 8th order accuracy in quadrature) with the transverse corrections presented in [30], combined which reaches 7th order overall accuracy formally. Nominally, the $R = 3$ scheme and the WENO-Z7 scheme have the same formal order of accuracy, although we see that the presented GP scheme with $R = 3$ supports finer scale features better than the WENO-Z7 counterpart.

Fig. 7 illustrates the differing jet morphologies that arise from different choices of stencil radius, length scale, and kernel function. First, one can observe that, for a fixed radius and length scale, the inverse quadratic kernel generally gives rise to finer scale features than the squared exponential kernel. Second, shorter length scales produce slightly more oscillatory solutions than longer length scales with the same stencil radius. Perhaps counter-intuitively, the shorter length scales do not appear to support meaningfully smaller scale features.

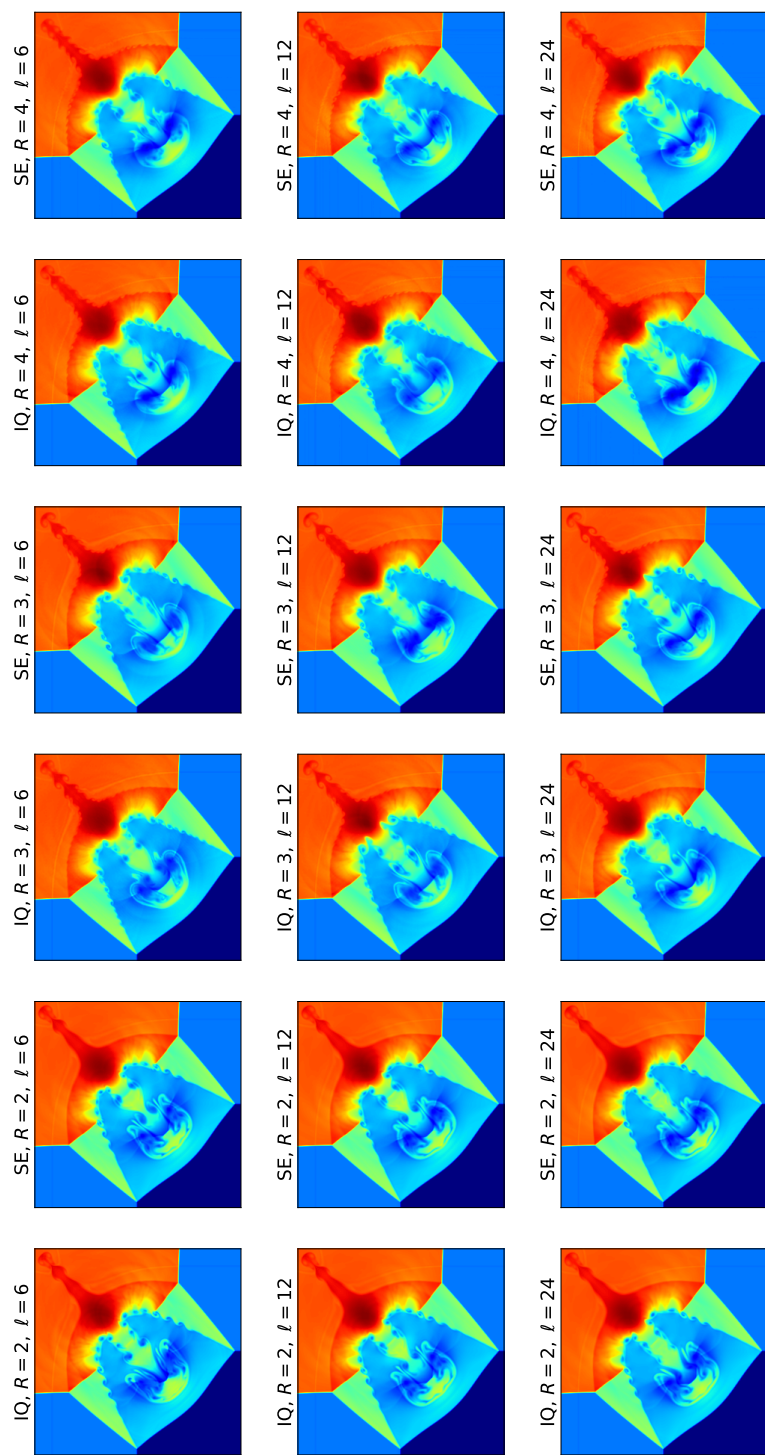


Figure 7: The final density fields for the third configuration 2D Riemann problem are shown for a variety of stencil radii, length scales, and kernel choices. Each panel has been zoomed into the region $[0.5, 0.87]^2$ and is solved using a grid resolution of 400×400 .

6.5. Richtmeyer-Meshkov instability

This benchmark problem evolves a Richtmeyer-Meshkov instability by passing a shock wave through a quiescent background with an oblique density jump. As the solution progresses, a secondary Kelvin-Helmholtz instability is excited, giving rise to fine-scale structures along the density jump interface. The initial conditions follow [64], and are

$$(\rho, u, v, P) = \begin{cases} \left(\frac{\gamma+1}{\gamma}, 2\sqrt{\gamma}, 0, \frac{3\gamma+1}{\gamma}\right), & x < 0.8, \\ (1, 0, 0, 1), & 0.8 < x < (y+1), \\ (3, 0, 0, 1), & \text{otherwise,} \end{cases} \quad (57)$$

where $\gamma = 1.4$. This condition launches a Mach 2 shock wave in the x -direction propagating through a stationary fluid with unit density and pressure. Further, into the preshock region, the density jumps by a factor of three across an interface angled at 45° . The domain is set as $\Omega = [0, 4] \times [0, 1]$. Reflecting boundary conditions are used on the top, bottom, and right sides of the domain, while outflow conditions are set on the left.

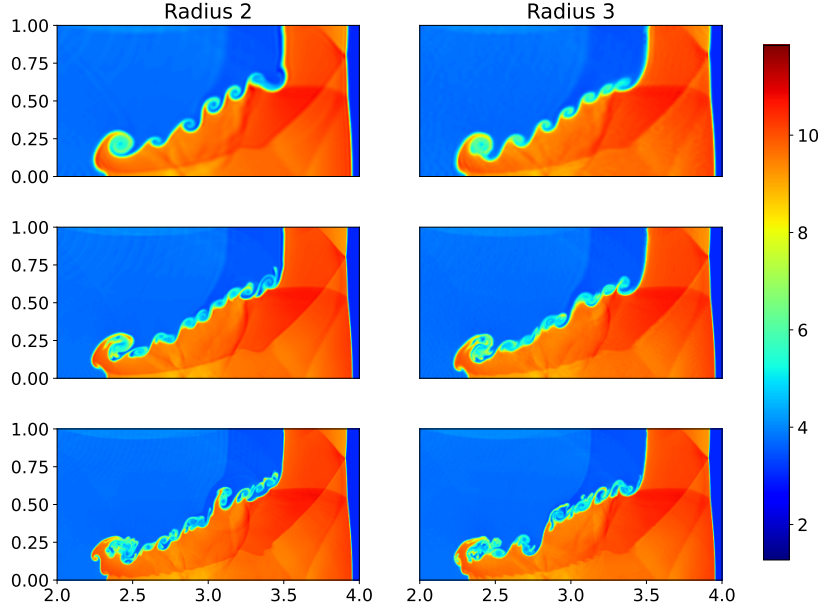


Figure 8: The density is shown at time $t_{\max} = 2$ for the Richtmeyer-Meshkov instability problem at several resolutions and stencil radii. The three rows correspond to mesh resolutions of 500×100 , 1000×200 , and 2000×400 , utilizing length scales of $\ell = 12\Delta x$, $24\Delta x$, and $48\Delta x$, respectively.

Fig. 8 shows the density at time $t_{\max} = 2$ for the Richtmeyer-Meshkov problem over a variety of mesh resolutions and stencil radii. In each case, the number of flux quadrature points on each face is set to $R + 1$ as before, and the RK-SSP(5,4) method is used for time integration under a CFL number of 0.75. As expected, we can see an

increasing level of vortical roll-ups and their fine structures along the interface as the order of accuracy increases from the 5th with $R = 2$ to the 7th with $R = 3$. This impact is greater on lower-resolution runs in particular, demonstrating the computational need for high-order methods that improve predictive capabilities in resolving fine-scale fluid structures with reduced numerical dissipation and consequently reduce numerical errors per grid resolution.

6.6. High Mach astrophysical jets

Testing code performance successfully on high Mach astrophysical jets has become a popular benchmark for assessing the positivity preservation capabilities of proposed methods. The huge kinetic energy incurred by the evolution of a high Mach jet can easily cause negative pressure and internal energy when converting from conserved variables. The propagation of strong shock waves introduces shear flows that further excite small-scale secondary Kelvin-Helmholtz instabilities. Numerically, the setup is also prone to the so-called carbuncle instability due to the shock front formation ahead of the grid-aligned jet evolution. These features together make simulating these problems tremendously challenging.

Several configurations have been considered for benchmark purposes in the literature, including the evolution of a single Mach 100 adiabatic light jet [57, 25], a single Mach 800 dense jet [57, 25, 70, 56], a collision of the light and dense jets [25], other non-magnetized and magnetized jets in Newtonian flow regimes [71, 70, 72], as well as relativistic jets in non-magnetized [73] and magnetized [74] configurations.

Here, we follow [57] to set up high and low-density jets at Mach 800 and Mach 100, respectively. In each case, the domain is set as $\Omega = [0, 1/2] \times [0, 3/2]$, with outflow conditions on the top and right sides, a reflecting condition on the left, and mixed inflow/outflow conditions on the bottom to introduce the jet. For the high-density jet, the domain is initially filled with quiescent gas with density $\rho = \frac{\gamma}{10}$ at unit pressure. For $x < 0.05$ along the bottom of the domain, the inflow conditions are $(\rho, u, v, P) = (\gamma, 0, 800, 1)$, making the jet density ten times higher than the ambient density. With the inflow jet condition of $(\rho, u, v, P) = (\gamma, 0, 100, 1)$, on the other hand, the low-density jet evolves into a quiescent denser background that has a constant unit pressure and a constant density of $\rho = 10\gamma$, making the penetrating jet ten times lighter than the background flow. Interested readers are referred to [25] for detailed discussions of the different flow structures of the two configurations and the relative challenges in simulating the low-density jet case.

Fig. 9 shows the logarithmic density at final times of $t_{\max} = 0.002$ and $t_{\max} = 0.04$ for the high- and low-density jets, respectively. The resolution is set to 400×1200 in all cases, the length scale is fixed at $\ell = 24\Delta x$, and the RK-SSP(5,4) time integrator is used under a CFL number of 0.75. The results are not only comparable to the published results but also demonstrate an increasing amount of fine-scale flow structures, which simultaneously validate the effectiveness of the positivity preservation scheme presented in Section 4 and the direct consequence of applying GP's high-order solutions that reduce numerical dissipation. These results are remarkably comparable to the recent positivity-preserving GP-MOOD results we presented in [25].

For this problem, we take extra care with choosing the number of quadrature points, $N_Q = 5$, i.e., fixing it as a constant value independent of R . We first recall that the

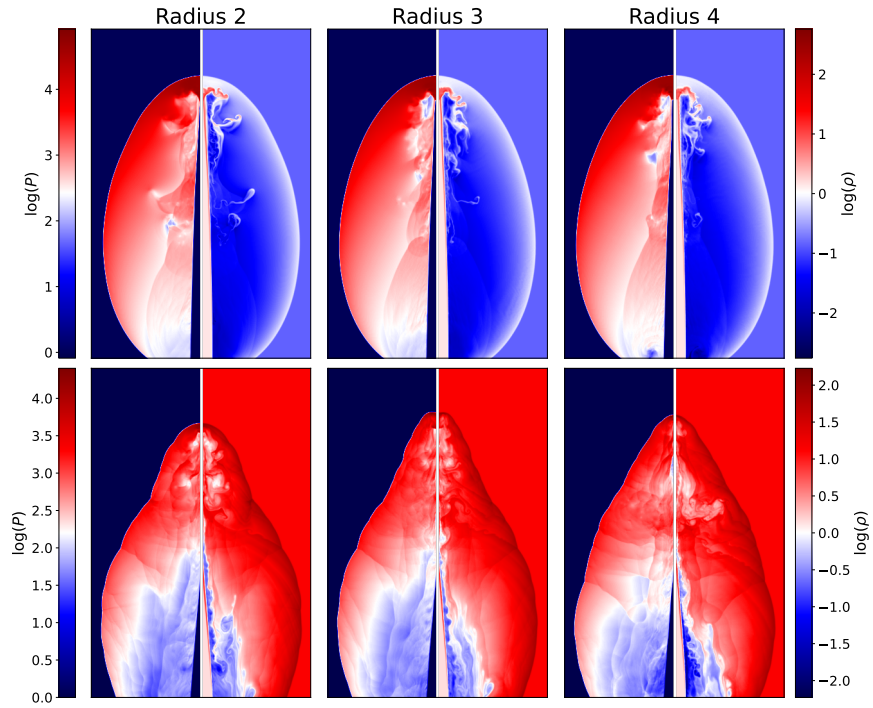


Figure 9: The top row shows $\log_{10} P$ and $\log_{10} \rho$ for the Mach 800 high-density jet at time $t_{\max} = 0.002$ for stencil radii $R = 2, 3$, and 4 from left to right. The bottom row shows the same for the Mach 100 low-density jet at time $t_{\max} = 0.04$. The left-half panel of each subfigure shows the logarithmic pressure using the colorbars on the left, and the right-half panel of each subfigure shows the logarithmic density colored according to the colorbars on the right. All cases use a grid resolution of 400×1200 , a length scale of $\ell = 24\Delta$, and five flux quadrature points, $N_Q = 5$.

positivity-preserving limiter operates directly on the Riemann states. In all other examples in this paper, the number of Riemann states, which is the same as N_Q , is determined by the default choice of $N_Q = R + 1$. This is a specific design choice for our GP methods to provide the matching order of accuracy between the calculation of flux quadrature and the spatial accuracy of the baseline GP schemes with different radii R . However, we see that the positivity-preserving switch in Section 4 is engaged much more actively in the high Mach jet problems than any other problems, which produces a set of incongruent simulation results (e.g., dissonant jet heights for different R) due to the highly sensitive nature of the problem to the choice of N_Q for each radius R . Fixing $N_Q = 5$ helps keep the overall jet evolution consistent for differing stencil radii, and hence becomes a special choice for these problems.

The results in Fig. 9 show that increasing the stencil radius for the high-density jet supports more complicated structures within the sloughed-off gas at the head of the jet. The cocoon and secondary structures within are mostly the same regardless of the stencil radius. The low-density jet has a more complicated evolution. As the jet proceeds upward, its core is compressed by the higher-density ambient fluid, eventually reaching a critical width and subsequently re-expanding. Each of the stencil radii realizes this critical radius at nearly the same position, though small discrepancies here ultimately lead to the total height of the jet differing at the final time. The structure of the cocoon is similar across the results with different stencil radii. Maintaining positivity in this problem is extremely challenging.

7. Conclusion

This paper proposes a multidimensional adaptive order WENO finite volume method using kernel-based GP reconstruction. The use of kernel-based reconstruction allows great flexibility in the choice of stencils and substencils in multiple spatial dimensions. We showed in this paper that our non-polynomial, kernel-based design simplifies the implementation of high-order finite volume schemes in multiple dimensions by reconstructing all pointwise Riemann states along cell boundaries *directly* from cell-average data, and eliminating the need to define boundary conditions for intermediate quantities as in modified dimension-by-dimension schemes.

Furthermore, alternative variables for reconstruction, dubbed linearized primitive variables, are proposed as a simplification over the use of characteristic variables. These are simpler to define and implement than characteristic variables. Crucially, these provide direction-independent information, which allows the same non-linear weights within the WENO method to be used for the reconstruction of all Riemann states. The calculation of these non-linear weights is the most expensive part of the whole scheme, so the use of these variables provides a significant reduction in computational cost. Paired with these new variables for reconstruction, we also propose a simple and effective fix for the preservation of the positivity of density and pressure in the compressible Euler equations.

Finally, the proposed scheme is evaluated against a variety of stringent and illustrative benchmark problems. The method simultaneously demonstrates high-order non-linear accuracy on smooth flows, robust behavior in the face of strong shocks, and minimal preference for grid-aligned phenomena over non-aligned phenomena.

8. Acknowledgments

This work was supported in part by the National Science Foundation under grant AST-1908834. We also acknowledge the use of the Lux supercomputer at UC Santa Cruz, funded by NSF MRI grant AST-1828315.

Appendix A. Integrated squared exponential kernel

The squared exponential kernel Eq. (16) can be analytically integrated for use in Eq. (12) and Eq. (13). We utilize the contour-Padé method to solve for the prediction vectors given in Eq. (15) so it is beneficial to first rewrite the kernel as

$$K_{se}(x, y; \epsilon) = e^{-\epsilon^2(x-y)^2}, \quad (\text{A.1})$$

where $\epsilon^2 = \frac{1}{2l^2}$ is the shape parameter. As mentioned in Section 3.1 it will be more useful to evaluate these integrals with respect to a grid with unit scale, in which case the shape parameter is normalized as $\hat{\epsilon} = \epsilon\Delta x$. The separable nature of the squared exponential kernel means that we need only present the 1-dimensional kernel. The entries of the sample vector are

$$\begin{aligned} [\mathbf{T}]_l &= \lambda_l^{(y)} K_{se}(x^*, y; \epsilon) \\ &= \frac{1}{\Delta x} \int_{x_{l-1/2}}^{x_{l+1/2}} e^{-\epsilon^2(x^*-y)^2} dy \\ &= \frac{\sqrt{\pi}}{2\hat{\epsilon}} [\text{erf}(\hat{\epsilon}(\Delta^* + 1/2)) - \text{erf}(\hat{\epsilon}(\Delta^* - 1/2))], \end{aligned} \quad (\text{A.2})$$

where $\Delta^* = \frac{x^*-x_l}{\Delta x}$ is the normalized signed distance from the reconstruction point to the center of the l^{th} cell. Similarly, the entries of the matrix \mathbf{C} are

$$\begin{aligned} [\mathbf{C}]_{hl} &= \lambda_h^{(x)} \lambda_l^{(y)} K_{se}(x, y; \epsilon) \\ &= \frac{1}{\Delta x^2} \int_{x_{h-1/2}}^{x_{h+1/2}} \int_{x_{l-1/2}}^{x_{l+1/2}} e^{-\epsilon^2(x-y)^2} dy dx \\ &= \frac{\sqrt{\pi}}{2\hat{\epsilon}} [(\Delta_{hl} + 1) \text{erf}(\hat{\epsilon}(\Delta_{hl} + 1)) + (\Delta_{hl} + 1) \text{erf}(\hat{\epsilon}(\Delta_{hl} + 1)) - 2\Delta_{hl} \text{erf}(\hat{\epsilon}\Delta_{hl})] \\ &\quad + \frac{1}{2\hat{\epsilon}^2} [e^{-\hat{\epsilon}^2(\Delta_{hl}+1)^2} + e^{-\hat{\epsilon}^2(\Delta_{hl}-1)^2} - 2e^{-\hat{\epsilon}^2\Delta_{hl}^2}], \end{aligned} \quad (\text{A.3})$$

where $\Delta^* = \frac{x_h-x_l}{\Delta x}$ is the normalized signed distance between the centers of the h^{th} and l^{th} cells.

References

- [1] S. Godunov, I. Bohachevsky, Finite difference method for numerical computation of discontinuous solutions of the equations of fluid dynamics, *Matematičeskij sbornik* 47 (1959) 271–306.

- [2] A. Harten, B. Engquist, S. Osher, S. R. Chakravarthy, Uniformly high order accurate essentially non-oscillatory schemes, iii, in: *Upwind and high-resolution schemes*, Springer, 1987, pp. 218–290.
- [3] A. Harten, Eno schemes with subcell resolution, *Journal of Computational Physics* 83 (1989) 148–184.
- [4] X.-D. Liu, S. Osher, T. Chan, Weighted essentially non-oscillatory schemes, *Journal of computational physics* 115 (1994) 200–212.
- [5] G.-S. Jiang, C.-W. Shu, Efficient implementation of weighted eno schemes, *Journal of computational physics* 126 (1996) 202–228.
- [6] R. Borges, M. Carmona, B. Costa, W. S. Don, An improved weighted essentially non-oscillatory scheme for hyperbolic conservation laws, *Journal of Computational Physics* 227 (2008) 3191–3211.
- [7] M. Castro, B. Costa, W. S. Don, High order weighted essentially non-oscillatory WENO-Z schemes for hyperbolic conservation laws, *Journal of Computational Physics* 230 (2011) 1766–1792.
- [8] D. Levy, G. Puppo, G. Russo, Central weno schemes for hyperbolic systems of conservation laws, *ESAIM: Mathematical Modelling and Numerical Analysis-Modélisation Mathématique et Analyse Numérique* 33 (1999) 547–571.
- [9] J. Qiu, C.-W. Shu, On the construction, comparison, and local characteristic decomposition for high-order central weno schemes, *Journal of Computational Physics* 183 (2002) 187–209.
- [10] J. S. Hesthaven, F. Mönkeberg, S. Zaninelli, RBF based CWENO method, in: S. J. Sherwin, D. Moxey, J. Peiró, P. E. Vincent, C. Schwab (Eds.), *Spectral and High Order Methods for Partial Differential Equations ICOSAHOM 2018*, Springer International Publishing, Cham, 2020, pp. 191–201.
- [11] J. Qiu, C.-W. Shu, Hermite WENO schemes and their application as limiters for Runge–Kutta discontinuous Galerkin method: one-dimensional case, *Journal of Computational Physics* 193 (2004) 115–135.
- [12] J. Qiu, C.-W. Shu, Hermite WENO schemes and their application as limiters for Runge–Kutta discontinuous Galerkin method II: Two dimensional case, *Computers & Fluids* 34 (2005) 642–663.
- [13] D. S. Balsara, S. Garain, C.-W. Shu, An efficient class of weno schemes with adaptive order, *Journal of Computational Physics* 326 (2016) 780–804.
- [14] A. K. Henrick, T. D. Aslam, J. M. Powers, Mapped weighted essentially non-oscillatory schemes: achieving optimal order near critical points, *Journal of Computational Physics* 207 (2005) 542–567.
- [15] H. Feng, F. Hu, R. Wang, A new mapped weighted essentially non-oscillatory scheme, *Journal of Scientific Computing* 51 (2012) 449–473.

- [16] H. Feng, C. Huang, R. Wang, An improved mapped weighted essentially non-oscillatory scheme, *Applied Mathematics and Computation* 232 (2014) 453–468.
- [17] R. Wang, H. Feng, C. Huang, A new mapped weighted essentially non-oscillatory method using rational mapping function, *Journal of Scientific Computing* 67 (2016) 540–580.
- [18] R. Li, W. Zhong, A modified adaptive improved mapped weno method, arXiv preprint arXiv:2011.03916 (2020).
- [19] R. Li, W. Zhong, Locally order-preserving mapping for weno methods, *Journal of Computational and Applied Mathematics* (2022) 115004.
- [20] A. Reyes, D. Lee, C. Graziani, P. Tzeferacos, A new class of high-order methods for fluid dynamics simulations using gaussian process modeling: One-dimensional case, *Journal of Scientific Computing* 76 (2018) 443–480.
- [21] A. Reyes, D. Lee, C. Graziani, P. Tzeferacos, A variable high-order shock-capturing finite difference method with GP-WENO, *Journal of Computational Physics* 381 (2019) 189–217.
- [22] P. McCorquodale, P. Colella, A high-order finite-volume method for conservation laws on locally refined grids, *Communications in Applied Mathematics and Computational Science* 6 (2011) 1–25.
- [23] D. S. Balsara, T. Rumpf, M. Dumbser, C.-D. Munz, Efficient, high accuracy adiweno schemes for hydrodynamics and divergence-free magnetohydrodynamics, *Journal of Computational Physics* 228 (2009) 2480–2516.
- [24] D. S. Balsara, Divergence-free reconstruction of magnetic fields and weno schemes for magnetohydrodynamics, *Journal of Computational Physics* 228 (2009) 5040–5056.
- [25] R. Bourgeois, D. Lee, GP-MOOD: A positivity-preserving high-order finite volume method for hyperbolic conservation laws, *Journal of Computational Physics* 471 (2022) 111603.
- [26] R. Zhang, M. Zhang, C.-W. Shu, On the order of accuracy and numerical performance of two classes of finite volume WENO schemes, *Communications in Computational Physics* 9 (2011) 807–827.
- [27] P. Buchmüller, C. Helzel, Improved accuracy of high-order WENO finite volume methods on Cartesian grids, *Journal of Scientific Computing* 61 (2014) 343–368.
- [28] D. Lee, H. Faller, A. Reyes, The piecewise cubic method (PCM) for computational fluid dynamics, *Journal of Computational Physics* 341 (2017) 230–257.
- [29] S. I. Reeves, D. Lee, A. Reyes, C. Graziani, P. Tzeferacos, An application of gaussian process modeling for high-order accurate adaptive mesh refinement prolongation, *Communications in Applied Mathematics and Computational Science* 17 (2022) 1–41.

- [30] P. Buchmüller, C. Helzel, Improved accuracy of high-order weno finite volume methods on cartesian grids, *Journal of Scientific Computing* 61 (2014) 343–368.
- [31] R. Schaback, H. Wendland, Kernel techniques: From machine learning to meshless methods, *Acta Numerica* 15 (2006) 543–639.
- [32] H. Wendland, *Scattered Data Approximation*, Cambridge Monographs on Applied and Computational Mathematics, Cambridge University Press, 2004. doi:[10.1017/CB09780511617539](https://doi.org/10.1017/CB09780511617539).
- [33] S. Clain, S. Diot, R. Loubère, A high-order finite volume method for systems of conservation laws—multi-dimensional optimal order detection (MOOD), *Journal of computational Physics* 230 (2011) 4028–4050.
- [34] S. Diot, S. Clain, R. Loubère, Improved detection criteria for the multi-dimensional optimal order detection (MOOD) on unstructured meshes with very high-order polynomials, *Computers & Fluids* 64 (2012) 43–63.
- [35] S. Diot, R. Loubère, S. Clain, The multidimensional optimal order detection method in the three-dimensional case: very high-order finite volume method for hyperbolic systems, *International Journal for Numerical Methods in Fluids* 73 (2013) 362–392.
- [36] S. Diot, La méthode MOOD Multi-dimensional Optimal Order Detection: la première approche a posteriori aux méthodes volumes finis d’ordre très élevé, Ph.D. thesis, Université de Toulouse, Université Toulouse III-Paul Sabatier, 2012.
- [37] W. Zhang, A. Almgren, V. Beckner, J. Bell, J. Blaschke, C. Chan, M. Day, B. Friesen, K. Gott, D. Graves, et al., Amrex: a framework for block-structured adaptive mesh refinement, *Journal of Open Source Software* 4 (2019) 1370–1370.
- [38] S. I. Reeves, D. Lee, A. Singh, K. Verma, A gaussian process upsampling model for improvements in optical character recognition, in: *International Symposium on Visual Computing*, Springer, 2020, pp. 263–274.
- [39] T. Sonar, Optimal recovery using thin plate splines in finite volume methods for the numerical solution of hyperbolic conservation laws, *IMA Journal of Numerical Analysis* 16 (1996) 549–581.
- [40] A. Reyes, D. Lee, C. Graziani, P. Tzeferacos, A new class of high-order methods for fluid dynamics simulations using gaussian process modeling: One-dimensional case, *Journal of Scientific Computing* 76 (2018) 443–480.
- [41] J. Guo, J.-H. Jung, A RBF-WENO finite volume method for hyperbolic conservation laws with the monotone polynomial interpolation method, *Applied Numerical Mathematics* 112 (2017) 27–50.
- [42] H. Liu, X. Jiao, Wls-eno: Weighted-least-squares based essentially non-oscillatory schemes for finite volume methods on unstructured meshes, *Journal of Computational Physics* 314 (2016) 749–773.

- [43] T. Aboiyar, E. H. Georgoulis, A. Iske, Adaptive order methods using kernel-based polyharmonic spline weno reconstruction, *SIAM Journal on Scientific Computing* 32 (2010) 3251–3277.
- [44] G. E. Fasshauer, M. J. McCourt, Kernel-based approximation methods using Matlab, volume 19, World Scientific Publishing Company, 2015.
- [45] G. E. Fasshauer, M. J. McCourt, Stable evaluation of gaussian radial basis function interpolants, *SIAM Journal on Scientific Computing* 34 (2012) A737–A762.
- [46] B. Fornberg, G. Wright, Stable computation of multiquadric interpolants for all values of the shape parameter, *Computers and Mathematics with Applications* 48 (2004) 853–867.
- [47] B. Fornberg, E. Lehto, C. Powell, Stable calculation of gaussian-based rbf-fd stencils, *Computers & Mathematics with Applications* 65 (2013) 627–637.
- [48] G. B. Wright, B. Fornberg, Stable computations with flat radial basis functions using vector-valued rational approximations, *Journal of Computational Physics* 331 (2017) 137–156.
- [49] G. Fasshauer, M. McCourt, Kernel-based Approximation Methods using MATLAB, WORLD SCIENTIFIC, 2015. URL: <https://www.worldscientific.com/doi/abs/10.1142/9335>. doi:10.1142/9335. arXiv:<https://www.worldscientific.com/doi/pdf/10.1142/9335>.
- [50] C. Rasmussen, C. Williams, Gaussian Processes for Machine Learning, Adaptive Computation And Machine Learning, MIT Press, 2005. URL: <http://books.google.com/books?id=vWtwQgAACAAJ>.
- [51] C. Bishop, Pattern recognition and machine learning (information science and statistics), 1st edn. 2006. corr. 2nd printing edn, Springer, New York (2007).
- [52] D. S. Balsara, S. Garain, C.-W. Shu, An efficient class of weno schemes with adaptive order, *Journal of Computational Physics* 326 (2016) 780–804.
- [53] M. Abramowitz, I. A. Stegun, R. H. Romer, Handbook of mathematical functions with formulas, graphs, and mathematical tables, 1988.
- [54] R. Borges, M. Carmona, B. Costa, W. S. Don, An improved weighted essentially non-oscillatory scheme for hyperbolic conservation laws, *Journal of Computational Physics* 227 (2008) 3191–3211.
- [55] M. Castro, B. Costa, W. S. Don, High order weighted essentially non-oscillatory weno-z schemes for hyperbolic conservation laws, *Journal of Computational Physics* 230 (2011) 1766–1792.
- [56] Y. Ha, C. L. Gardner, Positive scheme numerical simulation of high mach number astrophysical jets, *Journal of Scientific Computing* 34 (2008) 247–259.

- [57] D. S. Balsara, Self-adjusting, positivity preserving high order schemes for hydrodynamics and magnetohydrodynamics, *Journal of Computational Physics* 231 (2012) 7504–7517.
- [58] X. Y. Hu, N. A. Adams, C.-W. Shu, Positivity-preserving method for high-order conservative schemes solving compressible euler equations, *Journal of Computational Physics* 242 (2013) 169–180.
- [59] X. Zhang, C.-W. Shu, On positivity-preserving high order discontinuous galerkin schemes for compressible euler equations on rectangular meshes, *Journal of Computational Physics* 229 (2010) 8918–8934.
- [60] P. K. Smolarkiewicz, The multi-dimensional crowley advection scheme, *Monthly Weather Review* 110 (1982) 1968 – 1983.
- [61] G. A. Sod, A survey of several finite difference methods for systems of nonlinear hyperbolic conservation laws, *Journal of computational physics* 27 (1978) 1–31.
- [62] C.-W. Shu, Essentially non-oscillatory and weighted essentially non-oscillatory schemes for hyperbolic conservation laws, in: *Advanced numerical approximation of nonlinear hyperbolic equations*, Springer, 1998, pp. 325–432.
- [63] P. D. Lax, X.-D. Liu, Solution of two-dimensional riemann problems of gas dynamics by positive schemes, *SIAM Journal on Scientific Computing* 19 (1998) 319–340.
- [64] R. Samtaney, Suppression of the richtmyer–meshkov instability in the presence of a magnetic field, *Physics of Fluids* 15 (2003) L53–L56.
- [65] R. J. Spiteri, S. J. Ruuth, A new class of optimal high-order strong-stability-preserving time discretization methods, *SIAM Journal on Numerical Analysis* 40 (2002) 469–491.
- [66] S. J. Ruuth, Global optimization of explicit strong-stability-preserving runge-kutta methods, *Mathematics of Computation* 75 (2006) 183–207.
- [67] S. Kawai, Divergence-free-preserving high-order schemes for magnetohydrodynamics: An artificial magnetic resistivity method, *Journal of Computational Physics* 251 (2013) 292–318.
- [68] S. C. Spiegel, H. T. Huynh, J. R. DeBonis, A Survey of the Isentropic Euler Vortex Problem using High-Order Methods, *AIAA AVIATION Forum*, American Institute of Aeronautics and Astronautics, 2015. URL: <https://doi.org/10.2514/6.2015-2444>. doi:10.2514/6.2015-2444, 0.
- [69] N. Fleischmann, S. Adami, N. A. Adams, Numerical symmetry-preserving techniques for low-dissipation shock-capturing schemes, *Computers and Fluids* 189 (2019) 94–107.

- [70] K. Wu, C.-W. Shu, Provably positive high-order schemes for ideal magnetohydrodynamics: analysis on general meshes, *Numerische Mathematik* 142 (2019) 995–1047.
- [71] X. Zhang, C.-W. Shu, On positivity-preserving high order discontinuous galerkin schemes for compressible euler equations on rectangular meshes, *Journal of Computational Physics* 229 (2010) 8918–8934.
- [72] M. Liu, M. Zhang, C. Li, F. Shen, A new locally divergence-free wls-eno scheme based on the positivity-preserving finite volume method for ideal mhd equations, *Journal of Computational Physics* (2021) 110694.
- [73] K. Wu, H. Tang, High-order accurate physical-constraints-preserving finite difference weno schemes for special relativistic hydrodynamics, *Journal of Computational Physics* 298 (2015) 539–564.
- [74] K. Wu, C.-W. Shu, Provably physical-constraint-preserving discontinuous galerkin methods for multidimensional relativistic mhd equations, *Numerische Mathematik* 148 (2021) 699–741.